bioRxiv preprint doi: https://doi.org/10.1101/2024.10.22.619706; this version posted October 23, 2024. The copyright holder for this preprint (which was not certified by peer review) is the author/funder, who has granted bioRxiv a license to display the preprint in perpetuity. It is made available under aCC-BY-NC-ND 4.0 International license.

Mitochondrial fission controls astrocyte morphogenesis and organization in the cortex

Maria Pia Rodriguez Salazar[1], Sprihaa Kolanukuduru1[1,2], Valentina Ramirez[1,3], Boyu Lyu[4], Gabrielle Sejourne[1], Hiromi Sesaki[5], Guoqiang Yu[6,7], Cagla Eroglu[1,8,9,10*]

1 The Department of Cell Biology, Duke University Medical Center, Durham, NC, USA

2 The Department of Psychology and Neuroscience, University of North Carolina at Chapel Hill, Chapel Hill, NC, USA

3 The Department of Psychology and Neuroscience, Duke University, Durham, NC, USA

4 Bradley Department of Electrical and Computer Engineering, Virginia Polytechnic Institute and State University, Arlington, VA, USA

5 Department of Cell Biology, John Hopkins University School of Medicine, Baltimore, MD

6 Department of Automation, Tsinghua University, Beijing 100084, China

7 IDG/McGovern Institute for Brain Research, Tsinghua University, Beijing 100084, China

8 Aligning Science Across Parkinson's (ASAP) Collaborative Research Network, Chevy Chase, MD

9 The Department of Neurobiology, Duke University Medical Center, Durham, NC, USA

10 Howard Hughes Medical Institute, Duke University Medical Center, Durham, NC, USA

*Corresponding author: Cagla Eroglu: cagla.eroglu@duke.edu

Summary:

During cortical astrocyte morphogenesis, mitochondria decrease in size to populate distal astrocyte processes. Drp1-mediated mitochondrial fission is necessary for peripheral astrocyte process formation. Astrocyte-specific Drp1 loss induces astrocyte reactivity, disrupts cortical astrocyte organization, and dysregulates gap-junction protein Connexin 43 abundance.

bioRxiv preprint doi: https://doi.org/10.1101/2024.10.22.619706; this version posted October 23, 2024. The copyright holder for this preprint (which was not certified by peer review) is the author/funder, who has granted bioRxiv a license to display the preprint in perpetuity. It is made available under aCC-BY-NC-ND 4.0 International license.

ABSTRACT

Dysfunctional mitochondrial dynamics are a hallmark of devastating neurodevelopmental disorders such as childhood refractory epilepsy. However, the role of glial mitochondria in proper brain development is not well understood. We show that astrocyte mitochondria undergo extensive fission while populating astrocyte distal branches during postnatal cortical development. Loss of mitochondrial fission regulator, Dynamin-related protein 1 (Drp1), decreases mitochondrial localization to distal astrocyte processes, and this mitochondrial mislocalization reduces astrocyte morphological complexity. Functionally, astrocyte-specific conditional deletion of Drp1 induces astrocyte reactivity and disrupts astrocyte organization in the cortex. These morphological and organizational deficits are accompanied by loss of astrocytic gap junction protein Connexin 43. These findings uncover a crucial role for mitochondrial fission in coordinating astrocytic morphogenesis and organization, revealing the regulation of astrocytic mitochondria dynamics as a critical step in neurodevelopment.

bioRxiv preprint doi: https://doi.org/10.1101/2024.10.22.619706; this version posted October 23, 2024. The copyright holder for this preprint (which was not certified by peer review) is the author/funder, who has granted bioRxiv a license to display the preprint in perpetuity. It is made available under aCC-BY-NC-ND 4.0 International license.

INTRODUCTION

Mitochondria are dynamic organelles that move, divide, and fuse in response to changing cellular states (Friedman and Nunnari, 2014; Youle and van der Bliek, 2012). Localized functions of mitochondria within cells are governed by fusion, fission, and trafficking processes, collectively referred to as mitochondrial dynamics (Ni et al., 2015). Mitochondrial dynamics are particularly important for the function and development of highly compartmentalized cells such as neurons, where mitochondria within distal compartments perform key functions including ion buffering, energy production, and local protein translation (Billups and Forsythe, 2002; López-Doménech and Kittler, 2023; Rangaraju et al., 2019). Furthermore, distal mitochondria regulate cellular morphology of neurons through focalized ATP generation for actin polymerization at growth cones, and disruptions in mitochondrial dynamics result in stunted neurite growth (Courchet et al., 2013; Smith and Gallo, 2018; Steketee et al., 2012). Indeed, mutations in the genes that control the mitochondrial dynamics' machinery cause severe neurodevelopmental disorders, such as forms of childhood refractory epilepsy (Abati et al., 2022; Vanstone et al., 2016).

Despite the clear importance of mitochondrial dynamics in brain development, the role of this organelle in non-neuronal brain cells is less well understood. In particular, astrocytes are the most abundant glial cells in the brain and have highly ramified processes that make up more than half of the brain parenchyma by infiltrating the neuropil. These fine astrocyte processes interact with synapses, vasculature, and other glia (Allen and Lyons, 2018) where they regulate synapse formation, neurotransmitter and ion buffering, and maintain the blood-brain barrier (Alvarez et al., 2013; Chung et al., 2015). Intriguingly, astrocyte peripheral processes are loaded with mitochondria at higher densities than the surrounding neuropil (Lovatt et al., 2007), and their mitochondria are recruited to perisynapses in response to neuronal activity (Stephen et al., 2015), linking astrocyte mitochondrial dynamics and synapse function. Indeed, mature astrocyte mitochondria localize to functional microdomains in their arbors, where mitochondria regulate distal calcium dynamics to provide metabolic support in response to neuronal activity (Agarwal et al., 2017). Furthermore, recent work established that immature astrocytes have a high oxidative capacity and require mitochondrial biogenesis for proper morphogenesis and synapse formation (Zehnder et al., 2021). However, the role of mitochondrial dynamics in astrocyte development is unknown.

bioRxiv preprint doi: https://doi.org/10.1101/2024.10.22.619706; this version posted October 23, 2024. The copyright holder for this preprint (which was not certified by peer review) is the author/funder, who has granted bioRxiv a license to display the preprint in perpetuity. It is made available under aCC-BY-NC-ND 4.0 International license.

Beyond their morphological complexity, another way in which astrocytes regulate brain homeostasis is by tiling the entire brain parenchyma in evenly dispersed, non-overlapping domains. This organization enables astrocytes to form an extensive network that facilitates long-distance communication via gap junction-coupling between the distal processes of neighboring astrocytes (Bushong et al., 2002; Giaume et al., 2010). Tiling is absent in immature astrocytes, becomes established as astrocytes mature, and is regulated by the same machinery that ensures proper gap junction coupling via Connexin 43 (Cx43) (Baldwin et al., 2021). Cx43 is the most abundant gap junction protein in the brain and is almost exclusively expressed in astrocytes (Rash et al., 2001). Beyond its gap junction roles, Cx43 has cell-adhesion functions that drive astrocyte morphogenesis and migration (Kameritsch et al., 2012; Lagos-Cabré et al., 2019). Importantly, both tiling and gap junction-coupling are disrupted in many forms of brain injury and disease such as epilepsy and traumatic brain injury, indicating the importance of the proper establishment of astrocyte networks in brain homeostasis (Cheung et al., 2023; Clasadonte et al., 2017; Hösli et al., 2022; Oberheim et al., 2008).

Here, we investigated the role of mitochondrial dynamics in astrocyte morphogenesis, development, and function. We found that astrocyte mitochondria robustly increase in number and decrease in size to populate distal astrocyte processes during postnatal development, linking mitochondrial fission, to astrocyte morphogenesis. Dynamin-related protein 1 (Drp1), encoded by the gene *Dnm1l,* is a highly conserved GTPase that controls mitochondrial fission (Chang and Blackstone, 2010; Fonseca et al., 2019; Smirnova et al., 2001). Upon mitochondrial division, Drp1 recruited to the outer mitochondrial membrane to perform GTP hydrolysis-driven scission (Losón et al., 2013; Smirnova et al., 2001; Uo et al., 2009). Complete loss of Drp1 is embryonically lethal in mice (Wakabayashi et al., 2009b) and mutations in human *DNM1L* are linked to aggressive forms of developmental delay and childhood refractory epilepsy (Fahrner et al., 2016; Liu et al., 2021). Despite the causal link between Drp1 function and proper brain development, the role of Drp1 in astrocyte morphogenesis and development is unknown.

bioRxiv preprint doi: https://doi.org/10.1101/2024.10.22.619706; this version posted October 23, 2024. The copyright holder for this preprint (which was not certified by peer review) is the author/funder, who has granted bioRxiv a license to display the preprint in perpetuity. It is made available under aCC-BY-NC-ND 4.0 International license.

RESULTS

Mitochondria increase in number and decrease in size during cortical astrocyte morphogenesis

In mature astrocytes, mitochondria occupy the entirety of the astrocyte arbor (Lovatt et al., 2007) and this mitochondrial dispersion is remodeled in response to injury or disease (Gollihue and Norris, 2020; Motori et al., 2013). However, it is not well understood how the mitochondrial network is established and modified in developing astrocytes. Namely, how do mitochondrial transport, fission, or fusion dynamics orchestrate the distribution of astrocytic mitochondria during morphogenesis? To address this question, we first investigated how the mitochondrial network transforms during astrocyte maturation to populate the arbors. To do so, we used Postnatal Astrocyte Labeling by Electroporation (PALE) (Stogsdill et al., 2017) to fluorescently label sparse populations of astrocytes in the developing mouse V1 visual cortex. We used Mito-EGFP floxed mice (Agarwal et al., 2017), in which EGFP is targeted to the inner mitochondrial membrane protein cytochrome c oxidase, to label all mitochondria in Cre-expressing cells. We electroporated two plasmids into the ventricles of P0 mice— a pCAG-Cre plasmid to turn on the mitochondrial GFP and an mCherry-CAAX plasmid to label astrocyte membranes. Then using confocal microscopy, we imaged and analyzed astrocytes from layers 2/3, 4, and 5 of the developing visual cortex. This approach allowed us to visualize and quantify astrocyte morphology and their mitochondrial content throughout postnatal cortical development using confocal microscopy and morphometric analyses (Fig. 1A).

We focused our studies on the first 3 weeks of postnatal astrocyte development (P4, P7, P14, P21, Fig. 1B), because cortical astrocytes become morphological mature during this period (Clavreul et al., 2019; Stogsdill et al., 2017). As expected, astrocytes undergo robust growth and elaboration, increasing their overall cell volume approximately 20-fold between P4 and P21 (Fig. 1C). Concurrently, we found that total astrocyte mitochondrial volume per cell increased 5-fold between P4 and P14 and then remained constant between P14 and P21 (Fig. 1D). We next quantified total mitochondrial volume per cell normalized to astrocyte cell volume, hereafter referred to as total mitochondrial occupancy. We found total mitochondrial occupancy decreased during development due to the robust increase in astrocyte cell volume (Fig. 1E). Importantly, astrocyte mitochondria increased in number and decreased in size on average during these first two postnatal weeks (Fig.

bioRxiv preprint doi: https://doi.org/10.1101/2024.10.22.619706; this version posted October 23, 2024. The copyright holder for this preprint (which was not certified by peer review) is the author/funder, who has granted bioRxiv a license to display the preprint in perpetuity. It is made available under aCC-BY-NC-ND 4.0 International license.

1F-G), indicating mitochondria division (fission) occurs concurrently with astrocyte morphogenesis.

Mitochondria occupy fine astrocyte processes concurrently with morphogenesis *in vitro*

The recruitment of mitochondria to the distal edge of developing cell processes in other compartmentalized cells is required for cytoskeletal remodeling and branch outgrowth (Cunniff et al., 2016; Li et al., 2004; López-Doménech et al., 2016; Smith and Gallo, 2018; Steketee et al., 2012). However, the spatiotemporal distribution of mitochondria during astrocyte arborization and whether astrocyte mitochondria are present at the tips of their developing peripheral processes is not known. The highly complex morphology of astrocytes *in vivo* obstructs our ability to track and analyze individual astrocyte processes and their mitochondria. Therefore, we investigated how mitochondria are distributed throughout the astrocyte arbor during morphological growth using an *in vitro* astrocyte-neuron co-culture system. Astrocytes cultured on top of neurons gain a complex morphology compared to astrocytes cultured alone or with non-neuronal cells (Stogsdill et al., 2017). Thus, we used astrocyte-neuron co-cultures to stimulate astrocyte ramification and track how mitochondrial number, size, and distribution change during process elaboration. We isolated and transfected primary cortical rat astrocytes with cytosolic GFP and MitoDsRed constructs to label astrocytes and their mitochondria, respectively. Transfected astrocytes were then plated onto rat cortical neuron monolayers for 4, 12, 24, and 48 hours (Fig. 2A-B).

We developed a Matlab-based image analysis program, Seg_Astro (https://github.com/Eroglu-Lab/seg_cul_astro_app/tree/main) to quantify branch number, mitochondrial number, and mitochondrial size across astrocyte arbors. Seg_Astro uses branch width and branchpoints to determine the astrocyte branch hierarchy and assign four branch types: 1) soma and primary processes, 2) secondary processes, 3) fine processes, and 4) the terminal tips of processes (Fig. 2C). Seg_Astro then bins mitochondria into these 4 types of branches and outputs branch number, mitochondrial number, and mitochondrial size per branch type. We excluded mitochondrial measurements from the soma and primary branches of astrocytes as mitochondria form dense network in these compartments that cannot be distinguished as discrete mitochondria for number and size quantification.

bioRxiv preprint doi: https://doi.org/10.1101/2024.10.22.619706; this version posted October 23, 2024. The copyright holder for this preprint (which was not certified by peer review) is the author/funder, who has granted bioRxiv a license to display the preprint in perpetuity. It is made available under aCC-BY-NC-ND 4.0 International license.

Seg_astro quantification showed a significant increase across all astrocyte branch types (primary, secondary, fine, and terminal) between 4hr and 48hr in culture. Strikingly, astrocyte fine branches had the largest increase in number, quadrupling from 4 to 48 hours in culture (Fig 2D). Intriguingly, mitochondria were present across all astrocyte branch types including fine and terminal, as early as 4 hours and through 48 hours in co-culture (Fig. 2B Inset and 2E). These results show that mitochondria occupy distal processes during astrocyte branch development in vitro and suggest that mitochondrial recruitment to these distal processes may be required for sustained growth of astrocyte arbors.

Our analyses also revealed astrocyte mitochondria numbers increased across all branch types throughout time in culture, with fine branches housing the largest increase in number of mitochondria, 3-fold, by 48 hours in culture (Fig. 2E). While mitochondrial numbers increased, average mitochondrial size decreased across all astrocyte branch types throughout time in culture *except* in fine processes which housed small mitochondria throughout morphogenesis (Fig. 2F). This result suggested that mitochondrial fission may be required for mitochondrial recruitment to the growing fine/distal processes as there may be a maximum size threshold for mitochondria to occupy fine astrocyte branches. These data echo and expand upon our *in vivo* findings and implicate a role for mitochondrial division in distal astrocyte process morphogenesis.

Drp1-induced mitochondrial fission is required for distal astrocyte process formation and mitochondrial localization *in vitro*

Because cortical astrocyte morphogenesis occurred concurrently with extensive mitochondrial fragmentation *in vivo* and *in vitro*, we next investigated the role of mitochondrial fission in astrocyte development. We knocked down Drp1, the key GTPase regulator of mitochondrial fission (Smirnova et al., 2001) (Fig. 3A-B), in astrocytes using a small hairpin RNA (shRNA) targeting both the rat and mouse mRNAs (Sup. Fig. 2A-B) and assessed how it affected astrocyte morphological complexity in co-culture with neurons. We co-transfected GFP-expressing shDrp1 or a scrambled control shRNA (shControl) and MitoDsRed into astrocytes and co-cultured them on neurons for 48 hours. We used Seg_Astro to quantify mitochondrial and branch number per branch type in shControl and shDrp1 astrocytes (Fig. 3C). We found that Drp1 knockdown significantly decreased mitochondria numbers in secondary, fine, and terminal astrocyte processes

bioRxiv preprint doi: https://doi.org/10.1101/2024.10.22.619706; this version posted October 23, 2024. The copyright holder for this preprint (which was not certified by peer review) is the author/funder, who has granted bioRxiv a license to display the preprint in perpetuity. It is made available under aCC-BY-NC-ND 4.0 International license.

compared to control. The largest decrease in mitochondria numbers was in fine/distal branches, to less than 40% of shControl (Fig. 3D). Concurrently, shDrp1 astrocytes had a significant decrease of exclusively fine and terminal astrocyte process number compared to shControl. shDrp1 did not affect primary or secondary branch numbers (Fig. 3E). These data demonstrate that Drp1-induced mitochondrial fission is specifically required for fine and terminal astrocyte process formation, likely through regulation mitochondrial size and recruitment to these fine processes.

To determine if Drp1 GTPase activity-driven scission is necessary for its role in astrocyte distal process morphogenesis, we implemented human Drp1 constructs that are resistant to shDrp1 (Sup. Fig. 2A); wild-type human Drp1 (hDrp1) and GTPase-dead point mutant human Drp1 (hDrp1-K38E) (Fig. 3B) (König et al., 2021). The co-transfection of shDrp1 with hDrp1 rescued astrocyte distal process formation compared to shDrp1 alone, whereas the GTPase-dead counterpart could not (Fig. 3F-J). Together these data reveal that Drp1-mediated mitochondrial fission is necessary for the formation of fine/distal astrocyte branches *in vitro*. These data also suggest that mitochondrial recruitment to distal processes is facilitated by mitochondrial fission, and this recruitment is required for astrocyte fine branch formation and/or stabilization during astrocyte morphological growth.

Drp1 controls mitochondrial occupancy and distal astrocyte process morphogenesis *in vivo*

Because Drp1 is required for distal astrocyte branch formation *in vitro,* we next tested whether Drp1-mediated mitochondrial fission (Fig. 4A) would play a similar role in cortical astrocyte morphogenesis *in vivo.* To address this question, we used PALE to electroporate plasmids with shDrp1 or shControl into the ventricle of P0 Mito-EGFP floxed mice. These plasmids also express a membrane-tagged mCherry reporter, which we used to quantify astrocyte morphology. They were delivered together with a Cre-expressing plasmid, which drives Mito-EGFP expression to determine mitochondrial morphology at P21. We used Imaris to render 3D surfaces of astrocytes and their mitochondria and measure overall astrocyte territory size, the volume of distal neuropil-infiltrating astrocyte processes (Neuropil Infiltration Volume; NIV), and total mitochondrial volume in the whole astrocyte or the distal processes. Using these methods, we investigated how loss of Drp1 in cortical astrocytes *in vivo* impacted astrocyte territory size, distal process formation, and mitochondrial localization within the astrocyte arbors.

bioRxiv preprint doi: https://doi.org/10.1101/2024.10.22.619706; this version posted October 23, 2024. The copyright holder for this preprint (which was not certified by peer review) is the author/funder, who has granted bioRxiv a license to display the preprint in perpetuity. It is made available under aCC-BY-NC-ND 4.0 International license.

Interestingly, shDrp1 had no effect on astrocyte territory size or total mitochondrial content per cell (Fig. 4B, Sup. Fig. 2A-B). However, Drp1 knockdown significantly decreased mitochondrial localization to dital astrocyte regions, which was accompanied by a significant decrease in the volume of distal neuropil-infiltrating astrocyte processes (Fig. 4C-D). These results suggest that mitochondrial fission controls mitochondrial recruitment to distal/perisynaptic astrocyte processes which is required for proper neuropil infiltration by astrocytes *in vivo*.

To determine if distal astrocyte process formation was specifically controlled by Drp1-induced mitochondrial fission or a byproduct of modifying mitochondrial dynamics in general, we tested how disrupting mitochondrial fusion by knocking down Mitofusin1 or inhibiting mitochondrial transport by knocking down Miro1, modified astrocyte morphogenesis and mitochondrial occupancy. Mitofusin1 (Mfn1) is a GTPase on the outer membrane of mitochondria that facilitates fusion (Chen et al., 2003) (Fig. 4E). Miro1 is a GTPase adaptor that tethers the outer mitochondrial membrane to cytoskeletal motors for mitochondrial transport (Fransson et al., 2006) (Fig. 4I). We used PALE to electroporate shMfn1 or shMiro1 constructs (Sup. Fig. 1C-E). Interestingly, silencing Mfn1 caused a reduction in astrocyte territory size (Fig. 4F) but did not alter mitochondrial occupancy or the volume of distal neuropil-infiltrating processes (Fig. 4G-H, Sup. Fig. 2A, C), indicating mitochondrial fusion may play a role in astrocyte territory outgrowth independently of distal process complexity. Miro1 knockdown did not impact astrocyte morphology or total mitochondrial content (Fig. 4J-K, Sup. Fig. 2A, D) but caused an increase in the volume of mitochondria localized at the distal astrocyte processes (Fig. 4L), suggesting Miro1-mediated mitochondrial trafficking may regulate retrograde mitochondrial transport in developing astrocytes. Taken together, we found that mitochondrial dynamics are key regulators of astrocyte morphology, likely through the control of mitochondrial localization to nascent processes. Our findings show that astrocyte territory growth (large primary/secondary processes) does not require Drp1 function. However, Drp1-induced mitochondrial fission, but not mitochondrial fusion or transport, is necessary for the formation of distal neuropil-infiltrating astrocyte processes *in vivo.*

Drp1 is required for astrocyte organization during postnatal cortical development

During our PALE studies investigating the role of Drp1 in cortical astrocyte morphogenesis, we observed an unusual clustering phenotype in shDrp1-transfected astrocytes compared to shControl

bioRxiv preprint doi: https://doi.org/10.1101/2024.10.22.619706; this version posted October 23, 2024. The copyright holder for this preprint (which was not certified by peer review) is the author/funder, who has granted bioRxiv a license to display the preprint in perpetuity. It is made available under aCC-BY-NC-ND 4.0 International license.

at P21 (Fig. 5A). PALE time course experiments from P7-P21 revealed that shDrp1 astrocytes clustered as early as P7, and the clustering effect was cumulative across timepoints, reaching a nearly 4-fold increase in cluster area compared to control by P21 (Fig. 5B). To determine if this phenotype was due to a prolonged or exuberant astrocyte proliferation, we used Click-IT EdU chemistry to label proliferating cells in the cortex of PALE mice. shControl and shDrp1 plasmids were electroporated at P0, then EdU was injected intraperitoneally every two days from P3 to P13 and brains were collected 15 hours after EdU injection from P4 through P14 (Sup Fig. 3A). We did not find any evidence of increased or prolonged cell proliferation in shDrp1 transfected astrocytes compared to control (Sup. Fig. 3B, C), indicating astrocyte clustering in shDrp1-transfected astrocytes is not caused by over proliferation. These shDrp1 astrocyte clusters remained into adulthood (in 2 and 6-month-old mice, Sup. Fig. 3D, E), demonstrating astrocyte clustering due to Drp1 loss is not a transient developmental phenomenon that resolves after maturation.

Cortical astrocytes organize themselves into a network of evenly dispersed, non-overlapping domains, which is critical for proper brain function (Bushong et al., 2004). Because early postnatal loss of Drp1 led to cortical astrocyte clustering, we next sought to understand whether these astrocyte clusters displayed disrupted astrocyte organization. To do so, we measured the nearest neighbor distance between Sox9+ astrocyte nuclei to investigate whether shDrp1 astrocyte clusters consisted of adjacent astrocytes that maintained their evenly dispersed astrocyte organization (equidistant nuclei), or disorganized astrocytes with inconsistent nuclei distances (Fig. 5C). First, we found that Drp1 knockdown clusters contained ~4 nuclei on average compared to control astrocytes which only contain 1 nucleus (Fig. 5D), confirming that shDrp1-transfected astrocyte clusters comprised multiple astrocytes. Importantly, shDrp1 astrocyte clusters had a 3-fold decrease in nearest neighbor distance compared to control astrocytes (Fig. 5E), indicating a disorganization among cortical astrocytes when Drp1 is knocked down. These data show that loss of Drp1 impairs the astrocyte organization in the cortex by inducing clustering, suggesting Drp1 may play a role in the establishment of astrocyte tiling during development. Taken together these data demonstrate that Drp1-induced mitochondrial fission promotes both astrocyte morphogenesis and organization during postnatal development in the mouse cortex.

Astrocyte organization in the cortex is mechanistically linked to the formation of a gap junction-coupled astrocyte network (Baldwin et al., 2021). In particular, proper expression and localization

bioRxiv preprint doi: https://doi.org/10.1101/2024.10.22.619706; this version posted October 23, 2024. The copyright holder for this preprint (which was not certified by peer review) is the author/funder, who has granted bioRxiv a license to display the preprint in perpetuity. It is made available under aCC-BY-NC-ND 4.0 International license.

of Connexin 43 (Cx43) , the most abundant astrocytic gap junction protein (Dermietzel et al., 1991), is required for the establishment of non-overlapping astrocyte territories (Baldwin et al., 2021; Lagos-Cabré et al., 2019). Because we observed astrocyte disorganization and clustering in PALE shDrp1 astrocytes, we next wondered if loss of Drp1 caused these changes via disruption of gap junctions. To test this possibility, we quantified Cx43 via immunohistochemistry within shDrp1 and shControl PALE astrocytes. Strikingly, shDrp1 astrocytes had a 5-fold decrease in Cx43 with visible "holes" of Cx43 staining coinciding with the shDrp1 astrocyte clusters (Fig. 5F-G). These data reveal that Drp1 knockdown results in a profound reduction of Cx43 protein expression in astrocytes. Importantly, this effect of shDrp1 is Cx43-specific as we did not observe a change in the levels of Cx30, another gap junction protein which is also expressed by astrocytes (Sup. Fig. 3F). These results also suggest that Drp1-mediated Cx43 expression and/or localization may be responsible for the observed clustering phenotype of Drp1 knockdown astrocytes.

Astrocyte-specific Drp1 knock out induces astrocyte reactivity

To understand the impact of Drp1 loss in all astrocytes during cortical development, we utilized a conditional (floxed) allele of mouse Drp1 (Wakabayashi et al., 2009a) which we crossed with the tamoxifen-inducible astrocytic Cre-driver mouse Aldh1l1-CreERT2 (Srinivasan et al., 2016). A tdTomato-floxed reporter (Ai14) was also used to identify cells expressing Cre (Fig. 6A). To delete Drp1 from developing astrocytes, tamoxifen was injected into the milk spot of pups at P1, P2, and P3 and mice were collected for analyses at P21 (Fig. 6A). This approach resulted in a significant reduction of Drp1 protein in Drp1 conditional knock-out (cKO) astrocytes compared to wild-type control (cWT) by immunoblotting of isolated cortical astrocytes (Fig. 6B-C). Further, we found Drp1 protein reduced within Cre-positive ($tdTomato^{+}$) astrocytes across all cortical layers by immunohistochemistry, with an overall significant decrease in V1 cortex in Drp1 cKO astrocytes compared to control (Sup. Fig. 4A-C). These results show that Aldh1L1-CreERT2 driver along with daily tamoxifen injections between P1-P3 can be used to significantly reduce astrocytic Drp1 expression in mice *in vivo*.

Because we found that shDrp1 decreased astrocyte distal process formation and caused astrocyte clustering in our sparse PALE manipulation model, we wondered how global loss of Drp1 in astrocytes via conditional deletion would affect astrocyte development and cortical homeostasis.

bioRxiv preprint doi: https://doi.org/10.1101/2024.10.22.619706; this version posted October 23, 2024. The copyright holder for this preprint (which was not certified by peer review) is the author/funder, who has granted bioRxiv a license to display the preprint in perpetuity. It is made available under aCC-BY-NC-ND 4.0 International license.

We found an overall decrease in astrocyte density in the cortex by tdTomato$^+$ soma count that was primarily driven by decreases in L1 and L6 astrocytes in Drp1 cKO animals compared to control (Fig. 6D-E). The decrease in astrocyte density did not impact overall cortical thickness (Sup. Fig. 4D). Next, we quantified tdTomato$^+$ signal by immunohistochemistry as a proxy for astrocyte coverage and found that loss of Drp1 in cKO astrocytes significantly decreased their process coverage across the cortex compared to cWT, with the greatest coverage loss found in L5 and L6 astrocytes (Fig. 6F). Given that our astrocyte coverage analysis was normalized by astrocyte density, these data suggest this significant reduction in cortical astrocyte coverage is driven by the loss of astrocyte processes formation in Drp1 cKO.

Astrocytes modify their morphology and coverage of the cortex under disease and injury conditions (Fiebig et al., 2019; Oberheim et al., 2008). Furthermore, mature cortical astrocytes express low GFAP protein under homeostatic conditions but increase their GFAP expression upon entering a reactive state (Middeldorp and Hol, 2011). Because we found morphology and coverage abnormalities in astrocyte-specific Drp1 cKO mice, we next tested whether the astrocytes in these brains became reactive. To do so, we performed immunohistochemistry for GFAP in Drp1 cKO and cWT cortices, and quantified changes in their GFAP density and coverage (Fig. 6D). We found that Drp1 cKO mice had a significant increase in their cortical GFAP expression, as quantified by their density and coverage, predominantly in the mid layers (L2/3, L4, and L5) compared to control (Fig. 6G-H). In agreement, isolated astrocytes from Drp1 cKO mice showed increased expression of GFAP and vimentin mRNA, which are linked to astrocyte reactivity (Sup. Fig. 4E-F). These findings indicate a disruption in astrocyte homeostasis and suggest that conditional loss of Drp1 in astrocytes induces cortical astrocyte reactivity *in vivo*.

Astrocytic Drp1 loss dysregulates Connexin 43 expression *in vivo*

To determine if conditional deletion of Drp1 in cortical astrocytes disrupted astrocyte organization as we previously observed in our sparse PALE knockdown model (Fig. 5), we quantified both nearest neighbor and multiple neighbor distances between tdTomato$^+$ somas in the cortices of cKO and cWT mice (Fig. 7A). We found that in Drp1 cKO mice, astrocytes displayed significant decreases in nearest neighbor distance (Fig. 7B). Further, quantification of distances between multiple astrocyte neighbors revealed that Drp1 cKO astrocytes have a greater variability in

bioRxiv preprint doi: https://doi.org/10.1101/2024.10.22.619706; this version posted October 23, 2024. The copyright holder for this preprint (which was not certified by peer review) is the author/funder, who has granted bioRxiv a license to display the preprint in perpetuity. It is made available under aCC-BY-NC-ND 4.0 International license.

distances to their neighbors compared to cWT astrocytes (Fig. 7C), indicating Drp1 cKO astrocytes have an unevenly dispersed distribution of astrocyte somas compared to cWT. These data identify a disorganization in cortical astrocytes in the absence of Drp1. Taken together, these results are in line with our findings using shRNA constructs and PALE (Fig. 5) and show that loss of Drp1 in developing astrocytes disrupts cortical astrocyte organization *in vivo*.

Given the robust disruption to astrocyte organization in Drp1 cKO mice, we next tested how Cx43 expression was impacted in Drp1 cKO astrocytes compared to cWT. To do so, we stained for Cx43 in the cortex and found that Drp1 cKO astrocytes displayed a heterogeneous and uneven expression of Cx43, with some astrocytes apparently expressing almost no Cx43 while others expressed wild-type or higher levels of the protein compared to the more even distribution of Cx43 in cWT cortices (Fig. 7D). Indeed, quantification of Cx43 signal showed that while there was no change in average Cx43 expression between genotypes (Fig. 7E), there was significant increase in the variance of Cx43 expression in Drp1 cKO astrocytes compared to cWT (Fig. 7F). We quantified this heterogeneity by comparing the cumulative distribution and histogram of Cx43 expression per astrocyte and found that Drp1 cKO astrocytes had a significantly altered distribution of Cx43 expression (Fig. 7G). This heterogeneous expression of cortical Cx43 protein *in situ* led us to investigate how Cx43 mRNA and protein expression may be disrupted in astrocytes. To do so, we immunopurified astrocytes from the cortex and measured mRNA and protein levels of Cx43. Cx43 mRNA levels were unchanged in Drp1 cKO isolated astrocytes compared to cWT (Fig. 7H). Interestingly, immunoblotting for Cx43 in isolated astrocytes demonstrated a robust decrease of Cx43 full-length (FL) protein as well as its internally translated smaller isoforms in Drp1 cKO astrocytes compared to cWT (Fig. 7I). Importantly, the trafficking of Cx43-FL to the cell membrane to carry out its gap junction and cell-adhesion functions is regulated by its C-terminal isoform, Cx43-20k (Smyth and Shaw, 2013). Both Cx43-FL and Cx43-20k are significantly decreased in Drp1 cKO astrocytes compared to cWT (Fig. 7J-K). These findings indicate that loss of Drp1 dysregulates Cx43 protein, but not mRNA, expression in astrocytes *in vivo*. Taken together, these data suggest that Drp1-induced mitochondrial fission is required for proper Cx43 protein expression and the establishment of astrocyte organization in the cortex.

bioRxiv preprint doi: https://doi.org/10.1101/2024.10.22.619706; this version posted October 23, 2024. The copyright holder for this preprint (which was not certified by peer review) is the author/funder, who has granted bioRxiv a license to display the preprint in perpetuity. It is made available under aCC-BY-NC-ND 4.0 International license.

DISCUSSION

Astrocytes require a highly complex morphology to perform essential roles in brain development. They ramify into hundreds of thousands of fine processes enabling their functional interaction with neurons, synapses, neighboring astrocytes, and other brain cells. Distal mitochondria locally interact with the cytoskeleton to regulate branch morphology in compartmentalized cells such as neurons (Courchet et al., 2013; Smith and Gallo, 2018), but the roles of mitochondria in fine astrocyte processes are largely unknown. Mature astrocytes were historically believed to be predominantly glycolytic (Pellerin and Magistretti, 1994), not depending on mitochondrial respiration for their own survival (Supplie et al., 2017), and instead using their mitochondria to provide metabolic support for neurons (Pellerin et al., 1998). Indeed, astrocyte mitochondria have recently emerged as gatekeepers of several biological processes that maintain brain homeostasis including regulation of blood-brain barrier remodeling, neuroinflammation, and neurodegeneration (Göbel et al., 2019; Ignatenko et al., 2018; Motori et al., 2013; Popov et al., 2023). While these studies introduce astrocytic mitochondria as key regulators of brain function, the cell-intrinsic roles of mitochondria in astrocyte and brain development are not well understood.

Our findings elucidate a previously unknown role for mitochondrial fission in regulating distal astrocyte process morphogenesis and astrocyte organization in the developing mouse cortex. We show that astrocytes undergo robust mitochondrial division to predominantly occupy distal astrocyte processes during postnatal cortical development. Inhibiting mitochondrial fission by silencing Drp1, reduces mitochondrial occupancy of distal astrocyte processes and diminishes peripheral astrocyte branch formation specifically, without affecting overall astrocyte territory size or growth. Functionally, Drp1-induced mitochondrial fission and occupancy of distal astrocyte processes are essential for the establishment of an organized astrocyte network and proper expression of gap junction protein, Cx43. Finally, mitochondrial fission is critical for astrocyte homeostasis, as global Drp1 loss in developing astrocytes induces cortical astrocyte reactivity, indicating that mitochondrial fission, distal mitochondrial localization, and astrocyte fine process formation are required for proper astrocyte development.

Several recent studies have elucidated astrocyte-neuron and astrocyte-astrocyte cell adhesion-based mechanisms that instruct astrocyte morphogenesis (Baldwin et al., 2021; Stogsdill et al., 2017; Takano et al., 2020; Tan et al., 2023; Zipursky et al., 2024). Curiously, loss of these cell-

bioRxiv preprint doi: https://doi.org/10.1101/2024.10.22.619706; this version posted October 23, 2024. The copyright holder for this preprint (which was not certified by peer review) is the author/funder, who has granted bioRxiv a license to display the preprint in perpetuity. It is made available under aCC-BY-NC-ND 4.0 International license.

adhesions often concurrently disrupts both astrocyte territory formation and complexity of distal astrocyte processes. Here we identify an organelle-driven mechanism that regulates peripheral astrocyte process morphogenesis independently from the development of higher order astrocyte processes and overall astrocyte size. The specificity of mitochondrial fission in regulating distal astrocyte process development could be attributed to their actin-rich cytoskeletal make-up which is distinct from larger processes. Primary astrocyte processes, which determine territory size, contain mainly intermediate filaments and microtubules (Haseleu et al., 2013). In other cell types, local mitochondrial ATP has been shown to fuel actin polymerization (Cunniff et al., 2016). Thus, it is possible that mitochondrial fission facilitates the recruitment of mitochondria into actin-rich distal astrocyte processes to supply local ATP required for actin polymerization during morphogenesis. In the absence of mitochondrial fission, the mislocalization of mitochondria away from peripheral, fine astrocyte branchlets could impair actin-cytoskeleton dynamics during morphogenesis. Because these peripheral astrocyte processes are critical components of the tripartite synapse, future work is needed to elucidate the role of astrocyte mitochondrial fission in proper synapse formation and function.

Our study establishes the role of Drp1 and mitochondrial fission in astrocyte organization in the cortex as measured by the distances between astrocytic neighbors, and this disruption is likely accompanied by tiling defects. While the molecular mechanisms that drive astrocyte domain formation and tiling remain largely unknown, we know that proper organization of astrocyte networks is functionally necessary for brain development and health. A recent study identified an astrocyte-astrocyte cell-adhesion molecule, HepaCAM, that controls the establishment of non-overlapping astrocyte domains through cis interactions with neighboring astrocytes and regulation of Cx43 localization (Baldwin et al., 2021). In our study, both sparse knockdown and conditional deletion of Drp1 in astrocytes led to dysregulation of Cx43 protein expression and caused disrupted astrocyte organization in the cortex. These results support previous findings that both Cx43 abundance and stability are critical for the proper migration of astrocytes and even dispersion of the astrocyte network (Lagos-Cabré et al., 2019; Wiencken-Barger et al., 2007), and reveal this process is regulated at least in part by astrocyte mitochondrial fission during cortical development. Future work is needed to investigate whether cortical astrocyte disorganization in response to Drp1 loss is also accompanied by disrupted astrocyte territory overlap and gap junction coupling.

bioRxiv preprint doi: https://doi.org/10.1101/2024.10.22.619706; this version posted October 23, 2024. The copyright holder for this preprint (which was not certified by peer review) is the author/funder, who has granted bioRxiv a license to display the preprint in perpetuity. It is made available under aCC-BY-NC-ND 4.0 International license.

How could Drp1-induced mitochondrial fission regulate Cx43 protein levels in astrocytes? Previous studies in cardiac cells found that the C-terminus of Connexin 43 is internally translated to generate a small 20kDa Cx43 isoform (Cx43-20kDa), which is required for the trafficking of full-length Cx43 (Cx43-FL) to the cell membrane (Smyth and Shaw, 2013). Loss of Cx43-20kDa leads to degradation of mistrafficked Cx-43-FL (Xiao et al., 2020). Importantly, Cx43-20kDa can localize to the outer mitochondrial membrane and in conditions of mitochondrial stress, which cause mitochondrial elongation, Cx43-20kDa can abandon its canonical Cx43-FL trafficking roles and instead employ a Drp1-independent, actin-based mechanism to induce mitochondrial fission (Shimura et al., 2021). Our findings show that conditional deletion of Drp1 in isolated astrocytes diminished both FL and the 20kDa isoforms of Cx43 protein. Importantly, Cx43 mRNA is unaffected by Drp1 loss, indicating Drp1 regulation of Cx43 occurs independently of transcription. Therefore, it is possible Drp1 loss in astrocytes causes a similar redirection of Cx43-20kDa away from its Cx43-FL trafficking role in an attempt to aid mitochondrial fission, resulting in the degradation of mistrafficked Cx43-FL and astrocyte disorganization. Furthermore, Cx43-20kDa has been previously detected in astrocytes and overexpression of astrocytic Cx43-20kDa promotes neuronal survival and recovery in a rat model of traumatic brain injury (TBI) through unknown mechanisms (Ren et al., 2020). These recent studies coupled with our findings suggest the Cx43-20kDa/Drp1 axis may be critical not only in brain development, but also in brain disease and therapeutics.

Finally, this study has important implications for understanding the pathology of neurological diseases, particularly neurodevelopmental diseases with Drp1 dysfunction. For example, point mutations in human Drp1 cause encephalopathy due to defective mitochondrial and peroxisomal fission-1 (EMPF1), a devastating disorder that presents in a spectrum of varying severity including microcephaly, developmental delay, refractory epilepsy, and lethal infantile encephalopathy (Fahrner et al., 2016; Lhuissier et al., 2022; Liu et al., 2021; Vanstone et al., 2016). While much research has focused on the disruption of excitation/inhibition (E/I) balance and neuronal pathogenesis of EMPF1 (Casillas-Espinosa et al., 2012; Ke et al., 2023), our results reveal how Drp1 dysfunction in astrocytes alone can fundamentally disrupt cortical development through astrocyte morphogenesis and organization deficits. Decreased distal astrocyte process development could contribute to diminished tripartite synapse formation (Stogsdill et al., 2017), subsequently disrupting the E/I balance. Furthermore, while loss of astrocyte tiling has been

bioRxiv preprint doi: https://doi.org/10.1101/2024.10.22.619706; this version posted October 23, 2024. The copyright holder for this preprint (which was not certified by peer review) is the author/funder, who has granted bioRxiv a license to display the preprint in perpetuity. It is made available under aCC-BY-NC-ND 4.0 International license.

455 reported in models of epilepsy (Oberheim et al., 2008), it has been unclear whether the phenotype
456 is causative or a consequence of disease. Our findings suggest endogenous loss of astrocytic Drp1
457 is sufficient to cause astrocyte reactivity which is a hallmark of many neurological disorders,
458 underscoring the translational importance of astrocyte mitochondrial fission in neuropathology. In
459 future studies, it will be interesting to investigate whether astrocyte-specific Drp1 loss causes the
460 synaptic E/I imbalance deficits associated with human *DNM1L* mutations. In conclusion, we show
461 a novel role for Drp1-induced mitochondrial fission in astrocyte peripheral process morphogenesis
462 and in regulating the establishment of an organized astrocyte network, demonstrating astrocyte
463 mitochondria are essential instructors of proper brain development.

464

465

bioRxiv preprint doi: https://doi.org/10.1101/2024.10.22.619706; this version posted October 23, 2024. The copyright holder for this preprint (which was not certified by peer review) is the author/funder, who has granted bioRxiv a license to display the preprint in perpetuity. It is made available under aCC-BY-NC-ND 4.0 International license.

FIGURE LEGENDS

Fig.1: Mitochondria increase in number and decrease in size during cortical astrocyte morphogenesis *in vivo*. (A) Schematic of Postnatal Astrocyte Labeling by Electroporation (PALE). (B) Representative images of V1 astrocytes expressing mCherry-CAAX (magenta, top panels) and their EGFP mitochondria (green, bottom panels) at P4, P7, P14, and P21. Scale bar: 10 μm. Super-plots for the quantification of (C) astrocyte cell volume, (D) total mitochondrial volume per cell, (E) mitochondrial volume normalized to cell volume, (F) average mitochondrial number per cell, and (G) average mitochondrial size per cell from P4-P21. N=3-4 male and female mice/timepoint (large circled data points), n= 2-6 cells/mouse, 10-13 cells total/timepoint (small gray data points). Data are presented as mean ± SEM. Nested one-way ANOVA with Tukey post-hoc test.

Fig. 2: Mitochondria occupy fine astrocyte processes concurrently with astrocyte morphological arborization *in vitro*. (A) Schematic of astrocyte-neuron co-culture assay. (B) Representative images of rat astrocytes transfected with EGFP (green, top panels) and MitoDsRed (magenta, middle panels) from 4 to 48 hours in co-culture with cortical neurons. Inset (bottom panels) of distal astrocyte processes (green) housing mitochondria (magenta) at the leading edge of growing processes from 4 to 48 hours in culture. Scale bars: 20 μm. (C) Overview of Seg_Astro image analysis pipeline. (D) Astrocyte secondary, fine/distal, and terminal branch number at 4 vs. 48 hours in culture. n = 10-12 cells per timepoint from one experiment. Unpaired two-tailed t-test. (E) Total astrocyte mitochondria number, and (F) average mitochondrial size in secondary, fine/distal, and terminal astrocyte branches from 4 to 48 hours in culture. n = 10-12 cells per timepoint from one experiment. Data are presented as mean ± SEM. One-way ANOVA with Tukey post-hoc test.

Fig 3: Drp1-induced mitochondrial fission is required for fine astrocyte process formation and mitochondrial localization *in vitro*. (A) Schematic of Drp1 in mitochondrial fission. (B) Drp1 domain structure noting K38E mutation in the GTPase domain. (C) Representative images of rat astrocytes transfected with shRNA targeting Drp1 (shDrp1) or a scrambled control (shControl) (first column) co-cultured on neurons (unlabeled), and their mitochondria (second column) across primary, secondary, fine, and terminal astrocyte process types. Scale bar: 20μm. (D) Super-plotted quantification of average mitochondrial number in secondary, fine, and terminal

bioRxiv preprint doi: https://doi.org/10.1101/2024.10.22.619706; this version posted October 23, 2024. The copyright holder for this preprint (which was not certified by peer review) is the author/funder, who has granted bioRxiv a license to display the preprint in perpetuity. It is made available under aCC-BY-NC-ND 4.0 International license.

branches from shControl vs. shDrp1 astrocytes. (E) Quantification of primary, secondary, fine, and terminal branch numbers from shControl and shDrp1 astrocytes. Data are mean ± S.E.M. n = 4 independent experiments (large circles), 10 cells/condition/experiment (small gray dots). Nested t-test. (F) Representative images of rat astrocytes transfected with shControl (green), shDrp1 (green), shDrp1 (green)+ hDrp1-YFP (magenta), or shDrp1 (green)+ hDrp1-K38E-CFP (magenta. Scale bar: 40µm. (G) Quantification of total primary, (H) secondary, (I) fine, and (J) terminal branch number in astrocytes across the 4 conditions from (F). Data are mean ± S.E.M. n = 3 independent experiments (large circles), 10 cells/condition/experiment (small gray dots). Nested One-way ANOVA with Tukey post-hoc test.

Fig 4: Mitochondrial fission, not fusion nor transport, is required for distal astrocyte process morphogenesis *in vivo*. (A, E, I) Schematic of mitochondrial fission, fusion, and transport mediated by Drp1, Mfn1, and Miro1, respectively. (B-D, F-H, J-L) Representative images of V1 P21 astrocytes expressing mCherry-CAAX-tagged shRNA (magenta) against Drp1 (shDrp1), Mfn1 (shMfn1), Miro1, (shMiro1) or scrambled control (shControl) and their EGFP mitochondria (green). Scale bar, 10µm. (B, F, J) Astrocyte territory (cyan) and quantification, (D, G, K) NIV reconstructions (cyan) and quantification, and (D, H, L) distal mitochondrial volume (green within cyan ROI) and quantification in shControl, shDrp1, shMfn1, and shMiro1 conditions, respectively. N= 4-5 male and female mice/condition (large circles), n=2-4 cells/mouse, 10-15 cells total/condition (small gray dots). Data are mean ± S.E.M. Nested t-test.

Fig 5: Drp1 controls cortical astrocyte organization during postnatal development. (A) Representative images of V1 mouse cortices with astrocytes expressing mCherry-CAAX-tagged shRNA (magenta) against Drp1 (shDrp1) or scrambled control (shControl) and their EGFP mitochondria (green) at P7, P14, and P21. Scale bar, 200µm. (B) Quantification of astrocyte individual or cluster area per field of view at P7, P14, P21. N=3-4 male and female mice/condition (big circles), 3 cortical sections/mouse (small gray dots). Data points are mean ± S.E.M. Nested t-test. (C) Representative images of shControl (top) and shDrp1 (bottom) P21 astrocytes expressing mCherry-CAAX shRNAs (magenta) and stained with Sox9 (green). Yellow arrows note Sox9+ astrocytic nuclei within mCherry+ astrocytes. Scale bar, 40µm. (D) Quantification of number of Sox9+ astrocyte nuclei and (E) nearest neighbor distance between astrocytes per astrocyte cluster in P21 shControl and shDrp1 astrocytes. N=4-5 male and female mice/condition (large circles), n=2-6 cells or clusters/condition, 20 cells or clusters total/condition (small gray dots). Data are

bioRxiv preprint doi: https://doi.org/10.1101/2024.10.22.619706; this version posted October 23, 2024. The copyright holder for this preprint (which was not certified by peer review) is the author/funder, who has granted bioRxiv a license to display the preprint in perpetuity. It is made available under aCC-BY-NC-ND 4.0 International license.

mean ± S.E.M. Nested t-test. (F) Representative images of V1 astrocytes expressing mCherry-CAAX and shControl (top) and shDrp1 (bottom) stained with Cx43 (cyan) at P21. Scale bars, 20µm. (G) Quantification of Connexin43 expression within mCherry-CAAX astrocytes. N=6 male and female animals/condition (large circles), n=2-6 cells or clusters/animal, 20-25 cells total/condition (small gray dots). Data are mean ± S.E.M. Nested t-test.

Fig 6: Astrocyte-specific Drp1 cKO induces cortical astrocyte reactivity.

(A) Overview of astrocyte-specific conditional Drp1 knockout mouse breeding strategy and timeline of tamoxifen administration. (B) Representative immunoblot for Drp1 from immuno-purified astrocytes. COX4, a mitochondrial protein, serves as a loading control. (C) Quantification of Drp1 protein in isolated cKO and cWT astrocytes. N=3 mice/condition. Data are mean ± S.E.M. Unpaired, two-tailed t-test. (D) Representative images of Drp1 cWT and cKO V1 cortices at P21 with tdTomato$^+$ astrocytes (magenta, first column), stained for GFAP (green, second column), and merge (third column). Scale bar, 100µm. Zoom merge (last column). Scale bar, 20µm. (E) Quantification of cortical tdTomato$^+$ soma count of astrocyte density, (F) tdTomato$^+$ astrocyte coverage normalized to astrocyte density, (G) GFAP soma count, and (H) GFAP coverage normalized to astrocyte density per layer in Drp1 cKO compared to cWT. N=4 male and female mice/condition, 2-3 cortical images/mouse. Data are mean ± S.E.M. Two-way ANOVA with Sidak's multiple comparisons test.

Fig 7: Astrocytic Drp1 loss dysregulates astrocyte organization and Connexin 43 expression in the mouse cortex. (A) Diagram of astrocyte organization analysis by nearest and multiple neighbor distance quantification. (B) Violin plot of nearest neighbor average distance between tdTomato$^+$ somas across V1 cortex of Drp1 cWT and cKO mice. N=4 male and female mice/condition (large circles), ~200 distances per image, 2-3 cortical images/mouse. Data are mean ± S.E.M. Nested t-test. (C) Distribution of average distances to multiple (9) neighbors. N=4 male and female mice/condition, ~200 distances per image, 2-3 images/mouse. Kolmogorov-Smirnov test. (D) Representative images of Drp1 cWT and cKO V1 cortices with tdTomato$^+$ astrocytes (magenta) stained with Cx43 (cyan) at P21. Scale bar, 100µm. Quantification of (E) individual (F) variance, and (G) distribution of Cx43 mean gray value per astrocyte in Drp1 cKO and cWT mice. N=4 male and female mice/condition, n= 15-30 mid-layer astrocytes (L2/3, L4, L5) per animal from 2-3 section images/animal. Nested t-test for (E), Unpaired, two-tailed t-test

bioRxiv preprint doi: https://doi.org/10.1101/2024.10.22.619706; this version posted October 23, 2024. The copyright holder for this preprint (which was not certified by peer review) is the author/funder, who has granted bioRxiv a license to display the preprint in perpetuity. It is made available under aCC-BY-NC-ND 4.0 International license.

for (F), and Kolmogorov-Smirnov test for (G). (H) Quantification of Cx43 mRNA from isolated cKO and cWT astrocytes. N=4-6 mice/condition. Data are mean ± S.E.M. Unpaired two-tailed t-test. (I) Representative immunoblot of isolated astrocytes for Cx43 showing its full-length form at 40kDa and its 20kDa isoform using COX4 as loading control. (J) Quantification of full-length Cx43 protein, (K) Cx43-20kDa isoform protein in isolated cKO and cWT astrocytes. N=3 mice/condition. Data are mean ± S.E.M. Unpaired, two-tailed t-test.

Supplemental Figure 1: Validation of shRNA tools

(A) Schematic of shDrp1 sequence aligned to the mouse, rat, and human genome. **(B)** Drp1 relative mRNA expression in control and shDrp1 transfected mouse 3T3 cells. **(C)** Schematic of shMiro1 and shMfn1 sequences aligned to the mouse genome. **(B)** Miro1 and Mfn1 relative mRNA expression in control and shDrp1 transfected mouse 3T3 cells. Data are mean ±S.E.M. n = 3 independent experiments. Unpaired two-tailed t-test.

Supplemental Figure 2: Mitochondrial dynamics do not affect astrocyte total mitochondrial content

(A) Representative images of Imaris reconstructed V1 P21 astrocytes expressing mCherry-CAAX-tagged shRNA (magenta) against Drp1 (shDrp1), Mfn1 (shMfn1), Miro1, (shMiro1) or scrambled control (shControl) and their EGFP mitochondria (green). Scale bar, 10µm. **(B-D)** Quantification of total mitochondrial volume normalized to cell volume in shDrp1, shMfn1, and shMiro1 conditions, respectively. N=4-5 male and female mice/condition (large circles), n=2-4 cells/mouse, 10-15 cells total/condition (small gray dots). Data are mean ± S.E.M. Nested t-test.

Supplemental Figure 3: shDrp1-induced astrocyte clustering is not a result of increased astrocyte proliferation and is maintained through adulthood

(A) Overview of PALE combined with EdU labeling. **(B)** Representative images of V1 cortices with astrocytes expressing mCherry-CAAX shRNA (red) against Drp1 (shDrp1) or scrambled control (shControl) and EdU labeling (magenta) at P4 and P14. Scale bar, 200µm. **(C)** Quantification of Edu+ cells in shControl or shDrp1 cortices at P4, P8, P10, P12, and P14. N=3-4 male and female mice/condition, 3 cortical section images/mouse. Data points are timepoint averages ± S.E.M. Two-way ANOVA with Sidak's multiple comparisons test. **(D)** Representative images of V1 cortices with astrocytes expressing mCherry-CAAX shRNA (magenta) against Drp1

bioRxiv preprint doi: https://doi.org/10.1101/2024.10.22.619706; this version posted October 23, 2024. The copyright holder for this preprint (which was not certified by peer review) is the author/funder, who has granted bioRxiv a license to display the preprint in perpetuity. It is made available under aCC-BY-NC-ND 4.0 International license.

(shDrp1) or scrambled control (shControl) at 2 months and 6 months. Scale bar, 200µm. **(E)** Quantification of astrocyte cell or cluster area per field of view at 2 and 6 months. N=3 male and female mice/condition (large circles), 3 cortical section images/mouse (small gray dots). Data points are mean ± S.E.M. Nested t-test. **(F)** Representative images of V1 astrocytes from 3 mice per condition expressing mCherry-CAAX and shControl (top two rows) and shDrp1 (bottom two rows) stained with an antibody against Cx30 (cyan) at P21. Scale bars, 20µm.

Supplemental Figure 4: Astrocyte-specific Drp1 cKO mouse characterization

(A) Representative images of Drp1 cWT and cKO V1 cortices with tdTomato$^+$ astrocytes (magenta) stained with Drp1 (yellow) and showing Drp1 masked by tdTomato (last column) at P21. Scale Bar, 40µm. (B-C) Quantification of Drp1 mean gray value within tdTomato area normalized to astrocyte density per cortical layer (B) and across the whole cortex (C). N=3-4 male and female mice/condition, 2-3 cortical images/mouse. Data points are mean ± S.E.M. Two-way ANOVA with Sidak's multiple comparisons test for B, and Unpaired, two-tailed t-test for C. (D) Quantification of cortical thickness in Drp1 cKO compared to cWT mice. N=4 male and female mice/condition (large circles), n=2-3 cortical images/mouse (small gray dots). Data are mean ± S.E.M. Unpaired, two-tailed t-test. Quantification of (E) GFAP and (F) Vimentin mRNA from isolated cKO and cWT astrocytes. N=2-6 male and female mice/condition. Data are mean ± S.E.M. Unpaired two-tailed t-test.

bioRxiv preprint doi: https://doi.org/10.1101/2024.10.22.619706; this version posted October 23, 2024. The copyright holder for this preprint (which was not certified by peer review) is the author/funder, who has granted bioRxiv a license to display the preprint in perpetuity. It is made available under aCC-BY-NC-ND 4.0 International license.

MATERIALS AND METHODS

Resource availability

Further information and requests for resources and reagents should be directed to and will be fulfilled by Cagla Eroglu (cagla.eroglu@duke.edu).

Materials availability

The reagents generated in this study are available without restriction.

Data and code availability

The raw data and analyses generated during this study can be accessed on Zenodo at the following DOI: 10.5281/zenodo.13961281. The Seg_Astro code can be found at (https://github.com/Eroglu-Lab/seg_cul_astro_app/tree/main). Any additional information can be requested from the lead contact.

Animal studies

All mice and rats were used in accordance with the Institutional Animal Care and Use Committee (IACUC) and with oversight by the Duke Division of Laboratory Animal Resources (IACUC Protocol Numbers A117-20-05 and A103-23-04). All animals were housed under typical 12-hour light/dark cycles. Aldh1l1-Cre/ERT2 BAC transgenic (RRID:IMSR_JAX:029655) and ROSA-td-Tomato Ai14 (RTM) (RRID:IMSR_JAX:007914) lines were obtained through Jackson Laboratory. Wild-type CD1 mice (RRID: IMSR_CRL:022) used for PALE and CD1 (Sprague-Dawley) IGS rats (SD-001) used for primary culture preps were purchased from Charles River Laboratories. Rosa26-lsl-mito-EGFP (RRID:IMSR_JAX:021429) were previously described (Agarwal et al., 2017). Drp1 conditional knockout mice were previously described and were a gift from the Sesaki Laboratory (Wakabayashi et al., 2009a). Mice and rats of both sexes were included in all experiments. Sex was not an influence on any of the experimental outcomes.

Primary Cultures

Cortical Neuron Isolation and Culture Purified (glia-free) rat cortical neurons were prepared as described previously (Stogsdill et al., 2017). In brief, cortices from P1 rat pups of both sexes

bioRxiv preprint doi: https://doi.org/10.1101/2024.10.22.619706; this version posted October 23, 2024. The copyright holder for this preprint (which was not certified by peer review) is the author/funder, who has granted bioRxiv a license to display the preprint in perpetuity. It is made available under aCC-BY-NC-ND 4.0 International license.

(Sprague Dawley, Charles River Laboratories, SD-001) were micro-dissected, digested in papain (~7.5 units/mL) at 33°C for 45 minutes, triturated in low and high ovomucoid solutions, resuspended in panning buffer (DPBS (Gibco 14287) supplemented with BSA and insulin) and passed through a 20 µm mesh filter (Elko Filtering 03-20/14). Filtered cells were incubated on negative panning dishes coated with Bandeiraea Simplicifolia Lectin 1 (x2), followed by goat anti-mouse IgG+IgM (H+L) (RRID: AB_2338451), and goat anti-rat IgG+IgM (H+L) (RRID:AB_2338094) antibodies, then incubated on positive panning dishes coated with mouse anti-L1 (RRID:AB_528349) to bind cortical neurons. Adherent cells were collected by forceful pipetting with a P1000 pipette. Isolated neurons were pelleted (11 min at 200 g) and resuspended in serum-free neuron growth media (NGM; Neurobasal, B27 supplement, 2 mM L-Glutamine, 100 U/mL Pen/Strep, 1 mM sodium pyruvate, 4.2 µg/mL Forskolin, 50 ng/mL BDNF, and 10 ng/mL CNTF). 100,000 neurons were plated onto 12 mm glass coverslips coated with 10 µg/mL poly-D-lysine (PDL, Sigma P6407) and 2 µg/mL laminin and incubated at 37°C in 10% CO2. On day in-vitro (DIV) 2, half of the media was replaced with NGM Plus (Neurobasal Plus, B27 Plus, 100 U/mL Pen/Strep, 1 mM sodium pyruvate, 4.2 µg/mL Forskolin, 50 ng/mL, BDNF, and 10 ng/mL CNTF) and AraC (10 µM, Sigma, C1768) was added to stop the growth of proliferating contaminating cells. On DIV 3, all of the media was replaced with NGM Plus. Neurons were fed on DIV 6 and DIV 9 by replacing half of the media with NGM Plus. Detailed protocol can be found at (https://www.protocols.io/view/glia-free-cortical-neuron-culture-36wgq3r35lk5/v1)

Cortical Astrocyte Isolation and Culture Rat cortical astrocytes were prepared as described previously (Stogsdill et al., 2017). Briefly, P1 rat cortices from both sexes were micro-dissected, papain digested, triturated in low and high ovomucoid solutions, and resuspended in astrocyte growth media (AGM: DMEM (Gibco 11960), 10% FBS, 10 µM, hydrocortisone, 100 U/mL Pen/Strep, 2 mM L-Glutamine, 5 µg/mL Insulin, 1 mM Na Pyruvate, 5 µg/mL N-Acetyl-L-cysteine). Between 15-20 million cells were plated on 75 mm2 flasks (non-ventilated cap) coated with poly-D-lysine and incubated at 37°C in 10% CO2. On DIV 3, removal of non-astrocyte cells was performed by forcefully shaking closed flasks by hand for 10-15 seconds until only an adherent monolayer of astrocytes remained. AraC was added to the media from DIV 5 to DIV 7 to eliminate contaminating fibroblasts. On DIV 7, astrocytes were trypsinized (0.05% Trypsin-EDTA) and plated into 12-well or 6-well dishes. On DIV 8, cultured rat astrocytes were transfected

bioRxiv preprint doi: https://doi.org/10.1101/2024.10.22.619706; this version posted October 23, 2024. The copyright holder for this preprint (which was not certified by peer review) is the author/funder, who has granted bioRxiv a license to display the preprint in perpetuity. It is made available under aCC-BY-NC-ND 4.0 International license.

with shRNA and/or expression plasmids using Lipofectamine LTX with Plus Reagent (Thermo Scientific, 15338100) per the manufacturer's protocol. Briefly, 1 µg (12-well) or 2 µg (6-well) total DNA was diluted in Opti-MEM containing Plus Reagent, mixed with Opti-MEM containing LTX (1:2 DNA to LTX) and incubated for 30 minutes. The transfection solution was added to astrocyte cultures and incubated at 37°C for 3 hours. On DIV 10, astrocytes were trypsinized, resuspended in NGM plus, plated (20,000 cells per well) onto DIV 10 neurons, and co-cultured for 48 hours. Detailed protocol can be found at (https://www.protocols.io/view/astrocyte-isolation-and-acm-production-261gedp57v47/v1).

Cell Lines

3T3 3T3 cells (RRID:CVCL_0594) used for shRNA validation experiments were cultured in DMEM supplemented with 10% fetal bovine serum, 100 U/mL Pen/Strep, 2 mM L-Glutamine, and 1 mM sodium pyruvate. Cells were incubated at 37°C in 5% CO2 and passaged every 2-3 days.

Plasmids

shRNA plasmids pLKO.1 puro plasmids containing shRNA against mouse/rat *Drp1* (TRCN0000321170; CTATAATGCATGCACTATTTA) was generated in this study. shRNA sequence was obtained from RNAi Consortium (TRC) via Dharmacon. A scrambled shRNA sequence was generated (GTTCTAAGTTCCGTGTTCAGG) and cloned into the pLKO.1 TRC cloning vector (Moffat et al., 2006) according to Addgene protocols (https://www.addgene.org/protocols/plko/). To generate pLKO.1 shRNA plasmids that express EGFP, CAG-EGFP was removed from pLenLox-shNL1-CAG-EGFP (Chih et al., 2006) and inserted between Kpn1 and Spel sites in pLKO.1 Puro, replacing the puromycin resistance gene in pLKO.1. Final constructs generated were pLKO.1-scrambled-GFP (RRID: Addgene_228736) and pLKO.1-shDrp1-GFP (RRID: Addgene_228737).

PiggyBac plasmids pGLAST-PBase was a gift from Dr. Joseph Loturco (Chen and LoTurco, 2012). shRNA sequences against mouse/rat *Miro1* (TRCN0000330651; TGGACTGTGCTTCGACGATTT), *Mfn1* (TRCN0000081400; GCAAGATTACAGGAGTTTCAA), and *Drp1* (see above *shRNA plasmids*) were obtained from

bioRxiv preprint doi: https://doi.org/10.1101/2024.10.22.619706; this version posted October 23, 2024. The copyright holder for this preprint (which was not certified by peer review) is the author/funder, who has granted bioRxiv a license to display the preprint in perpetuity. It is made available under aCC-BY-NC-ND 4.0 International license.

RNAi Consortium (TRC) via Dharmacon. A scrambled shRNA sequence was generated (see above *shRNA plasmids*). To insert the hU6 promoter and shRNA in pPBCAG-mCherry-CAAX a DNA fragment containing hU6 and shRNA was amplified from pLKO.1-shRNA using Phusion High-Fidelity DNA Polymerase (NEB) with primers that introduced SpeI restriction sites (Forward Primer: GGACTAGTCAGGCCCGAAGGAATAGAAG; Reverse Primer: GGACTAGTGCCAAAGTGGATCTCTGCTG). PCR products were purified, digested with SpeI, and ligated into pPBCAG-mCherry-CAAX at the SpeI restriction site. An analytical digest with EcoRI followed by sequencing was used to confirm the orientation of the inserted DNA fragment. Final plasmids generated were pPB-scrambled-mCherry-CAAX (RRID: Addgene_228738), pPB-sDrp1-mCherry-CAAX (RRID: Addgene_228739), pPB-shMiro1-mCherry-CAAX (RRID: Addgene_228741), and pPB-shMfn1-mCherry-CAAX (RRID: Addgene_228740).

Other plasmids hDrp1-YFP and hDrp1-K38E-CFP were gifts from Heidi McBride (König et al., 2021) . Mito-DsRed was acquired from Addgene (RRID: Addgene_55838).

Biochemical assays

mRNA extraction and cDNA preparation Cells stored in TRIzol (#15596026; Invitrogen) were brought to room temperature and resuspended in a final volume of 1 ml of TRIzol. 200 µl of chloroform was added to each sample and mixed thoroughly. Samples were centrifuged at 12,000 g for 15 min at 4°C for phase separation and the clear aqueous phase was collected. 2 µl of GlycoBlue Coprecipitant (15 mg/ml, #AM9515; Invitrogen) and 500 µl of isopropanol were added to each sample, centrifuged at 12,000 g for 10 min at 4°C, precipitating RNA as a blue pellet. The RNA pellet was rinsed in 75% ethanol, air-dried, and resuspended in 20 µl of nuclease-free water. mRNA concentration in each sample was quantified via Qubit RNA HS Assay Kit (#Q32852; Invitrogen). RNA samples were then diluted with nuclease-free water to match concentrations across all samples. cDNA libraries were then generated by incubating the samples with qScript cDNA SuperMix (#101414-102; VWR) and nuclease-free water for 5 min at 25°C, 30 min at 42°C, and 5 min at 85°C. The resulting cDNA was then diluted appropriately with nuclease-free water and stored at −80°C.

bioRxiv preprint doi: https://doi.org/10.1101/2024.10.22.619706; this version posted October 23, 2024. The copyright holder for this preprint (which was not certified by peer review) is the author/funder, who has granted bioRxiv a license to display the preprint in perpetuity. It is made available under aCC-BY-NC-ND 4.0 International license.

Real-time qPCR cDNA samples were plated in duplicate on a 96-well qPCR plate and incubated with Fast SYBR Green Master Mix (#4385616; Applied Biosystems), nuclease-free water, and the forward and reverse primers of interest at a ratio of 5 µl SYBR: 3 µl water: 0.5 µl forward primer: 0.5 µl reverse primer: 1 µl sample. Each sample was plated twice to ensure technical replicates. A no-cDNA sample (water with primers and Master Mix) served as a negative control. Cycle threshold values were collected for each well and normalized to PPIA as a housekeeping gene. The sequences of forward (F) and reverse (R) primers used (5′→ 3′) are:
Drp1: (F) TTACGGTTCCCTAAACTTCACG and (R) GTCACGGGCAACCTTTTACGA
Miro1: (F) TGGGCAGCACTGATAGAATAGA and (R) GCAAAGACCGTAGCACCAAAG
Mfn1: (F) CCTACTGCTCCTTCTAACCCA and (R) AGGGACGCCAATCCTGTGA
Cx43: (F) ACAGCGGTTGAGTCAGCTTG and (R) GAGAGATGGGGAAGGACTTGT
GFAP: (F) GGGGCAAAAGCACCAAAGAAG and (R) GGGACAACTTGTATTGTGAGCC
Vimentin: (F) CGTCCACACGCACCTACAG and (R) GGGGGATGAGGAATAGAGGCT
PPIA: (F) GAGCTGTTTGCAGACAAAGTTC and (R) CCCTGGCACATGAATCCTGG

Protein extraction and western blotting Protein was extracted from cultured cells using RIPA lysis buffer (ThermoFisher, 89900). Cells were washed twice with ice-cold DPBS and incubated on ice in RIPA buffer for 5 minutes with occasional agitation. Cell lysates were collected, vortexed briefly, and centrifuged at 4°C at high speed for 10 minutes to pellet non-solubilized material. The supernatant was collected and stored at −80°C. To collect protein from astrocytes from Drp1 *cWT* and *cKO* mice at P21, astrocytes were isolated following a modified version of the Magnetic Activated Cell Sorting (MACS) protocol previously described (Holt et al., 2019). In brief, mice were anesthetized with 200 mg/kg tribromoethanol (avertin) and perfused with TBS/Heparin, cortices rapidly dissected, digested in papain (~7.5 units/mL) at 33°C for 45 minutes with pipette trituration every 15 minutes. Then homogenates were resuspended in Magnetic Activated Cell Sorting (MACS) buffer (0.002M EDTA, 0.2% milk peptone, 0.01M HEPES pH 7, 0.5% Glucose, 1X HBSS), and passed through a CellTrics 30 µm filter (Sysmex, 04-004-2326). Cortical cells were then cleared from microglia by incubating with anti-CD11b human/mouse magnetic microbeads (Miltenyi Biotec, 130-093-634) for 10 minutes at 4°C with rotation and passed through an LS separation column (Miltenyi Biotec, 130-042-401) inserted into a Quadro MACS Multi Stand magnetic stand (Miltenyi Biotec) followed by 3 washes with MACS buffer. Flowthrough

bioRxiv preprint doi: https://doi.org/10.1101/2024.10.22.619706; this version posted October 23, 2024. The copyright holder for this preprint (which was not certified by peer review) is the author/funder, who has granted bioRxiv a license to display the preprint in perpetuity. It is made available under aCC-BY-NC-ND 4.0 International license.

was then spun down and resuspended in MACS buffer and incubated with blocking buffer and anti-ACSA2 mouse magnetic microbeads (Miltenyi Biotec, 130-097-678) for 30 minutes at 4°C with rotation to isolate astrocytes. Cell suspension was again passed through a separation column inserted into a magnetic stand, rinsed 3 times with MACS buffer and column retentate (ACSA2+ population, astrocytes) was pelleted. Supernatant was discarded and astrocyte pellet was resuspended in RIPA buffer containing protease inhibitors (Roche, 4693132001) and incubated with rotation at 4°C for 20 minutes. Lysate was centrifuged at max speed at 4°C for 10 minutes, supernatant collected and stored at −80°C.

Pierce Micro BCA Protein Assay Kit (Thermo Fisher, 23235) was used to determine protein concentration, and lysates were subjected to western blot analysis and quantification using a SimpleWestern Jess (ProteinSimple) automated immunoassay system with a 12-230kDa Chemiluminescence Separation module (SM-W001) and associated manufacturer's protocol. Primary antibodies used were: anti-Drp1 (Rabbit,1:10, RRID: AB_2895215), Connexin43 (Rabbit, 1:10, RRID:AB_2294590), COX4 (Rabbit, 1:10, RRID:AB_443304).

Immunocytochemistry

Astrocyte-neuron co-cultures on glass coverslips were fixed on DIV 12 with warm 4% PFA for 7 minutes, washed 3 times with PBS, blocked in a blocking buffer containing 50% normal goat serum (NGS) and 0.4% Triton-X 100 for 30 minutes, and washed in PBS. Samples were then incubated overnight at 4°C in primary antibodies diluted in blocking buffer containing 10% NGS. Primary antibodies used were: anti-GFP (Chicken, 1:1000, RRID:AB_10000240) and anti-RFP (Rabbit, 1:1000, RRID:AB_2209751). Cells were then washed with PBS, incubated in Alexa-Fluor conjugated secondary antibodies (Life Technologies) for 2 hours at room temperature, and washed again in PBS. Coverslips were mounted onto glass slides with Vectashield mounting media containing DAPI (Vector Labs, H-1200-10), sealed with nail polish, and imaged on a BZ-X800 microscope (Keyence). Images of astrocytes were acquired at 40x magnification in red, green, and/or DAPI channels using a CCD camera. Astrocytes that contained a single nucleus as revealed by DAPI stain, strongly expressed fluorescent markers, and were not overlapping with other labeled astrocytes, were selected for imaging.

bioRxiv preprint doi: https://doi.org/10.1101/2024.10.22.619706; this version posted October 23, 2024. The copyright holder for this preprint (which was not certified by peer review) is the author/funder, who has granted bioRxiv a license to display the preprint in perpetuity. It is made available under aCC-BY-NC-ND 4.0 International license.

Astrocyte branch number and mitochondrial localization were analyzed using Seg_Astro MATLAB plugin. To quantify branch and mitochondrial number and size across the astrocyte arbor, Seg_Astro (https://github.com/Eroglu-Lab/seg_cul_astro_app/tree/main) first detects the astrocyte as well as the mitochondria by identifying locally significant regions based on order statistics(Wang et al., 2020). Specifically, for the detection of the astrocyte, due to the nonuniform intensity inside the cell, the initial detection contained many fragments. We further refined the detection by searching for the globally optimal linkage, which is based on the graph design that each node represents a fragment and the edge weight between nodes represents the mean intensity of the brightest path between each pair of fragments. Then, the optimal linkage was obtained by finding the min-spanning tree of the graph. Once the astrocyte is detected, Seg_Astro then uses branch width and branchpoints to determine the astrocyte branch hierarchy and assign four types of astrocyte branches per cell: 1) soma and primary processes, 2) secondary processes, 3) fine processes, and 4) the terminal tips of processes (Fig. 2C). Seg_Astro then bins mitochondria into these 4 branch types and outputs branch number, mitochondrial number, and mitochondrial size per branch type. Importantly, we excluded mitochondrial measurements from the soma and primary branches of astrocytes as mitochondria form a dense network in these compartments that cannot be distinguished as discrete mitochondria for number and size quantification. Image acquisition and analysis were performed blinded to experimental conditions. Each independent experiment consisted of primary neurons and astrocytes isolated from a unique litter of wild-type rats of mixed sexes. The exact number of independent experiments and the exact number of cells analyzed are indicated in the figure legend for each experiment. Branch and mitochondrial number per conditions were statistically analyzed using nested t-test or nested one-way ANOVA on Graphpad Prism 9.

Postnatal Astrocyte Labeling by Electroporation (PALE)

Late P0/early P1 mice were sedated by hypothermia until anesthetized and 1 µL of plasmid DNA mixed with Fast Green Dye was injected into the lateral ventricle of one hemisphere using a pulled glass pipette. For mCherryCAAX labeling and shRNA knockdown experiments in pups from mito-EGFP mice crossed with wild-type CD1 mice, the 1 µL of DNA contained 0.8 µg of pGLAST-PBase, 0.7 µg of pPB-shRNA-mCherryCAAX, and 0.5 µg of pCAG-Cre (RRID: Addgene_13775). Following DNA injection, electrodes were oriented with the positive terminal

bioRxiv preprint doi: https://doi.org/10.1101/2024.10.22.619706; this version posted October 23, 2024. The copyright holder for this preprint (which was not certified by peer review) is the author/funder, who has granted bioRxiv a license to display the preprint in perpetuity. It is made available under aCC-BY-NC-ND 4.0 International license.

above the visual cortex and the negative terminal below the chin, and 5 discrete 50 msec pulses of 100 V spaced 950 msec apart were applied. Pups were recovered on a heating pad, returned to their home cage, and monitored until collection at P4, P7, P14, P21, P60, or P180. In the case of plasmid expression in CD1 mice, assignment to experimental groups was randomly determined for each litter. The number of replicates for each experiment is indicated in the figure legends. All animals that appeared healthy at the time of collection were processed for data collection. All brain sections were examined for the presence of electroporated cells before staining and downstream analyses.

Tamoxifen administration

Tamoxifen (Sigma, T5648) was dissolved in corn oil (Sigma, 8267) at a concentration of 10 mg/mL and further diluted in corn oil to 1.25 mg/mL. 40 µL of the tamoxifen solution was injected into the milk spot using an insulin syringe, for a dose of 0.05 mg at P1, P2, and P3. Two tamoxifen injections (P1 and P2) were sufficient turn on tdTomato expression in all astrocytes, however a third dose of tamoxifen (at P3) was needed for achieving a significant decrease of Drp1 levels in astrocytes.

EdU administration

EdU stock solution from Click-iT EdU Imaging Kit (Thermofisher, C10640) was diluted in DPBS to a concentration of 10µM (2.5µg of EdU/µl). At timepoints noted in Supplemental Figure 4, pups were weighed and injected with 15µg of EdU per gram of animal weight (6µl of working 10µM EdU stock solution per gram of animal weight). Animals were collected for staining 16 hours after EdU injection and tissue sections were stained following the Click-iT EdU Imaging Kit manufacturer protocol.

Immunohistochemistry

Sample Preparation Mice used for immunohistochemistry were anesthetized with 200 mg/kg tribromoethanol (avertin) and perfused with TBS/Heparin and 4% PFA. Brains were collected and post-fixed in 4% PFA overnight, cryoprotected in 30% sucrose, frozen in a solution containing 2 parts 30% sucrose and 1 part TissueTek O.C.T. (Sakura Finetek, cat#4583) and stored at −80°C. Floating coronal tissue sections of 30, 40, 100 µm thickness were collected and stored in a 1:1

bioRxiv preprint doi: https://doi.org/10.1101/2024.10.22.619706; this version posted October 23, 2024. The copyright holder for this preprint (which was not certified by peer review) is the author/funder, who has granted bioRxiv a license to display the preprint in perpetuity. It is made available under aCC-BY-NC-ND 4.0 International license.

mixture of TBS/glycerol at −20°C. For immunostaining, sections were washed in 1x TBS containing 0.2% Triton-X 100 (TBST), blocked in 10% NGS diluted in TBST, and incubated in primary antibody for 2-3 nights at 4°C with shaking. Primary antibodies used were: anti-RFP (Rabbit, 1:2000, RRID:AB_2209751), GFP (Chicken, 1:2000, RRID:AB_10000240), Sox9 (Rabbit, 1:2000, RRID:AB_2239761), Connexin43 (Rabbit, 1:100, RRID:AB_2294590), Drp1 (Mouse, 1:100, RRID:AB_398424), Connexin30 (Rabbit, 1:500, RRID:AB_2533979), and GFAP (Rabbit, 1:1000, RID:AB_10013382). Following primary incubation, sections were washed in TBST, incubated in Alexa-Fluor conjugated secondary antibodies diluted 1:200 (Life Technologies) for 2-3 hours at room temperature, washed with TBST, and mounted onto glass slides using a homemade mounting media (90% Glycerol, 20 mM Tris pH 8.0, 0.5% n-Propyl gallate) and sealed with nail polish. For primary antibodies produced in mouse, isotype specific secondary antibodies were always used (e.g. goat anti-mouse IgG1) to avoid excessive background staining. For DAPI staining, DAPI (1:50,000) was added to the secondary antibody solution for the final 10 minutes of incubation. Images were acquired on a Stellaris 8 Leica microscope.

Astrocyte territory volume analysis To assess the territory volume of individual astrocytes in the developing mouse cortex, 100 µm-thick floating sections containing V1 astrocytes labeled sparsely via PALE with mCherry-CAAX and mito-EGFP were collected. High magnification images containing an entire astrocyte (50-60 µm Z-stack) were acquired on the Olympus FV 3000 microscope with the 60x objective. Criteria for data inclusion required that the entirety of the astrocyte could be captured within a single brain section, and that the astrocyte was located in layers 2/3, 4, or 5 of the visual cortex. Astrocytes in which the entire astrocyte could not be captured within the section or were located in other layers or outside of the visual cortex were excluded from the study and not imaged. Imaged astrocytes were analyzed using Imaris Bitplane software as described previously (Stogsdill et al., 2017). Briefly, surface reconstructions were generated and the Imaris Xtensions “Visualize Surface Spots” and “Convex Hull” were used to create an additional surface render representing the territory of the astrocyte. The volume of each territory was recorded, and astrocyte territory sizes from biological replicates were analyzed across experimental conditions using a nested t-test. The number of mice and cells/mouse analyzed are specified in the figure legend for each experiment.

bioRxiv preprint doi: https://doi.org/10.1101/2024.10.22.619706; this version posted October 23, 2024. The copyright holder for this preprint (which was not certified by peer review) is the author/funder, who has granted bioRxiv a license to display the preprint in perpetuity. It is made available under aCC-BY-NC-ND 4.0 International license.

Neuropil infiltration volume analysis To measure the extent of astrocyte infiltration into the neuropil, 60x high magnification Z-stack images with 2x optical zoom were acquired from mCherry-CAAX and mito-EGFP labeled astrocytes in 40 µm brain sections. Criteria for inclusion required the astrocyte to be located within layer 2/3, 4, or 5 of the visual cortex, express the fluorescent label, include their soma in the z-stack capture, and have at least 15µm in the z-dimension contained within the section. Astrocytes that did not meet these criteria were excluded from the study and not imaged. For each astrocyte, three ROIs (12.65 µm x 12.65 µm x 10 µm) containing the neuropil, and devoid of cell soma, large branches, and end feet were chosen and reconstructed using the surface tool in Imaris. The surface volume of each ROI was calculated and the three data points from each astrocyte were averaged. Data from biological replicates were analyzed using a nested t-test. The number of mice and cells/mouse analyzed are specified in the figure legend for each experiment.

Mitochondrial volume analysis To measure mitochondrial volume within whole astrocytes or distal astrocyte process, astrocyte images were captured as described above in *Astrocyte territory volume analysis* (for whole astrocyte mitochondrial volume) or *Neuropil infiltration volume analysis* (for distal NIV mitochondrial volume). In Imaris, the astrocyte volume rendered above was used to mask the mitochondrial EGFP channel. Either whole or distal mitochondria were reconstructed using the surface volume tool in Imaris. Data from biological replicates were analyzed using a nested t-test. The number of mice and cells/mouse analyzed are specified in the figure legend for each experiment.

Quantification of astrocyte cell or cluster area To analyze astrocyte cell or cluster area of sparse Drp1 knockdown PALE experiments, three 40µm sections per animal were imaged in 10x on the Olympus FV 3000 and loaded into ImageJ. The astrocyte mCherry channel, the RFP channel, was selected. The image was then stacked into a max projection z-stack and a gaussian blur of sigma radius 1.00 was applied. A threshold was then applied to the image to include signal from astrocytes in the cortex above the subventricular zone. Then, using ImageJ analysis, the area of each cluster above 500 pixels per image was recorded. The average cluster area per image was calculated and 3 technical replicates per animal were averaged for analysis. Data from biological replicates were analyzed using a nested t-test. The number of mice and cells/mouse analyzed are specified in the figure legend for each experiment.

bioRxiv preprint doi: https://doi.org/10.1101/2024.10.22.619706; this version posted October 23, 2024. The copyright holder for this preprint (which was not certified by peer review) is the author/funder, who has granted bioRxiv a license to display the preprint in perpetuity. It is made available under aCC-BY-NC-ND 4.0 International license.

Nearest and multiple neighbor analysis To measure the distance between astrocyte neighbors in sparse Drp1 knockdown PALE experiments, 63x images of astrocytes or astrocyte clusters from 40µm sections were captured on the Leica Stellaris 8 Confocal and loaded into ImageJ. Composite images merging the DAPI channel for all nuclei, Sox9 channel for astrocytic nuclei, and the RFP channel for astrocytes were generated. Using the line tool, a line was manually drawn from the edge of one Sox9+ nucleus within mCherry to the closest Sox9+ nucleus and the length of the line was measured. Each distance between neighbors was recorded from the same animal as technical replicates. Data from biological replicates were analyzed using a nested t-test. To quantify the number of Sox9+ nuclei, the composite images from above were used, and the number of Sox9+ nuclei within mCherry signal was manually counted. The number of Sox9+ nuclei per cell or cluster were recorded as technical replicates per mouse. The number of mice and cells/mouse analyzed are specified in the figure legend for each experiment. In the Drp1 conditional deletion mouse model, V1 cortical images of 30µm sections were taken on the Leica Stellaris 8 Confocal at 20x with 0.75 optical zoom. Single optical section images were loaded onto Imaris with a z-size of 0.01 µm. Selecting the tdTomato channel, soma spots were generated with an estimated XY diameter of 7.5 µm and with background subtraction using Imaris Spots tool. Object-Object statistics were collected for the spots generated. Once these soma spots were generated, distance to nearest neighbor and average distance to 9 neighbors were analyzed. Data from biological replicates were analyzed using a nested t-test and Kolmogorov-Smirnov test. The number of mice and cells/mouse analyzed are specified in the figure legend for each experiment.

Connexin43 volume analysis To quantify the amount of Connexin43 within astrocytes in the sparse Drp1 knockdown PALE model, 93x images (0.5 µm z-step, 10 µm z-stacks) from 40µm sections of astrocytes or clusters were taken on the Leica Stellaris 8 Confocal. Criteria for inclusion required the astrocyte to be located within layer 2/3, 4, and 5 of the visual cortex, express the fluorescent label, and have at least 10µm in the z-dimension contained within the section. For each astrocyte or astrocyte cluster, the Imaris surface tool was used to render the astrocyte volume. This astrocyte volume was then used to mask the Cx43 channel, and then Imaris surface tool was used to generate surface volumes of Cx43 puncta within the astrocyte volume territory only. Data from biological replicates were analyzed using a nested t-test. The number of mice and cells/mouse analyzed are specified in the figure legend for each experiment.

bioRxiv preprint doi: https://doi.org/10.1101/2024.10.22.619706; this version posted October 23, 2024. The copyright holder for this preprint (which was not certified by peer review) is the author/funder, who has granted bioRxiv a license to display the preprint in perpetuity. It is made available under aCC-BY-NC-ND 4.0 International license.

Astrocyte density analysis For quantifying the density of astrocytes in the Drp1 conditional deletion model, V1 cortical images of 30µm sections were taken on the Leica Stellaris 8 Confocal at 20x with 0.75 optical zoom. Using the tdTomato channel on ImageJ, a rectangular region of interest (ROI) that encompassed all cortical layers of the visual cortex was selected and saved to the ROI manager in ImageJ. Within the multi-layer rectangular ROI, ROIs for each cortical layer were drawn and saved. The area of each ROI was recorded. These imaging parameters and ROIs were also used for the *Cortical Astrocyte coverage analysis* and *Drp1 protein expression analyses by immunohistochemistry* below. The 'Show-all' feature on the ROI manager was selected, so that the boundaries between cortical layers were shown. Using the Cell Counter plug-in, tdTomato+ somas were manually counted. The number of somas across the cortex was calculated as the sum of tdTomato+ somas in all cortical layers. Density of tdTomato+ somas was calculated by dividing the number of tdTomato+ somas by their corresponding ROI area. GFAP+ cell density was calculated and analyzed in the same manner, using the GFAP channel instead of the tdTomato channel. Three sections were analyzed as technical replicates per mouse. Data from biological replicates were analyzed using a two-way ANOVA with Sidak's multiple comparisons test. The number of mice and cells/mouse analyzed are specified in the figure legend for each experiment.

Cortical Astrocyte coverage analysis To quantify astrocyte coverage across the cortex in the Drp1 conditional deletion model, cortical images were captured and divided into multiple ROIs for analysis as described above in *Astrocyte density analysis*. Using the threshold tool in ImageJ, the tdTomato channel coverage was binarized and saved as a tdTomato mask. Then, selecting each cortical ROI, the area of tdTomato coverage from the mask generated across the cortex and per layer was collected. tdTomato coverage was defined as the percent of tdTomato+ area divided by the density of tdTomato+ cells. GFAP coverage was calculated and analyzed in the same manner, using the GFAP channel instead of the tdTomato channel. GFAP coverage likewise normalized by tdTomato density. Three sections were analyzed as technical replicates per mouse. Data from biological replicates were analyzed using a two-way ANOVA with Sidak's multiple comparisons test. The number of mice and cells/mouse analyzed are specified in the figure legend for each experiment.

Drp1 protein expression analyses by immunohistochemistry For quantifying Drp1 protein levels in the Drp1 conditional deletion model, cortical images were captured and divided into multiple

bioRxiv preprint doi: https://doi.org/10.1101/2024.10.22.619706; this version posted October 23, 2024. The copyright holder for this preprint (which was not certified by peer review) is the author/funder, who has granted bioRxiv a license to display the preprint in perpetuity. It is made available under aCC-BY-NC-ND 4.0 International license.

ROIs for analysis as described above in *Astrocyte density analysis*. Then a mask of the tdTomato channel was applied to the Drp1 channel and mean gray value of Drp1 within astrocytes was collected per layer and across the cortex using ImageJ. The collected values were normalized to tdTomato+ soma density. Three sections were analyzed as technical replicates per mouse. Data from biological replicates were analyzed using a two-way ANOVA with Sidak's multiple comparisons test. The number of mice and cells/mouse analyzed are specified in the figure legend for each experiment.

Cx43 protein expression analysis by immunohistochemistry To measure Cx43 protein levels in astrocytes in the Drp1 conditional deletion model, cortical images were captured as described above in *Astrocyte density analysis*. ImageJ was used to subtract background from the Cx43 channel with a rolling ball radius of 50 units. Following background subtraction, individual astrocytes within layers 2/3, 4, or 5 were outlined with the freehand tool using tdTomato to determine astrocyte territories, and astrocyte outlines were saved as ROIs. Astrocyte ROIs were applied to Cx43 channel and the mean gray value of Cx43 signal was collected per astrocyte and normalized by the ROI area. Three sections were analyzed as technical replicates per mouse. Data from biological replicates were analyzed using a nested t-test, Kolmogorov-Smirnov test. The number of mice and cells/mouse analyzed are specified in the figure legend for each experiment.

Cortical thickness analysis: To measure cortical thickness in Drp1 cWT and cKO mice, 10x images of V1 cortices were taken on the Leica Stellaris 8 confocal. Images were loaded into ImageJ and the line tool was used to record length. Three lines per section were drawn from the subventricular zone to the Pia. The lengths of these lines were averaged per section for 3 sections per mouse, and data from each section was plotted as a technical replicate per mouse. Data from biological replicates were analyzed using a nested t-test.

Quantification and statistical analysis

All statistical analyses were performed using Graphpad Prism 9. The exact number of replicates, specific statistical tests, and P values for each experiment are indicated in the figures and figure legends. All data are represented as mean ± SEM, and individual data points are shown for all data, where applicable. Where indicated, nested t-tests were applied with an alpha threshold of 0.05 for

bioRxiv preprint doi: https://doi.org/10.1101/2024.10.22.619706; this version posted October 23, 2024. The copyright holder for this preprint (which was not certified by peer review) is the author/funder, who has granted bioRxiv a license to display the preprint in perpetuity. It is made available under aCC-BY-NC-ND 4.0 International license.

977 adjusted P-value. A Geisser-Greenhouse correction was used for both One-way and Two-way
978 ANOVA analyses. All experimental animals that appeared healthy at the time of tissue collection
979 were processed for data collection. Specific details for inclusion, exclusion, and randomization are
980 included in the specific subsections of the Materials and methods details section.

981

bioRxiv preprint doi: https://doi.org/10.1101/2024.10.22.619706; this version posted October 23, 2024. The copyright holder for this preprint (which was not certified by peer review) is the author/funder, who has granted bioRxiv a license to display the preprint in perpetuity. It is made available under aCC-BY-NC-ND 4.0 International license.

ACKNOWLEDGMENTS

We thank Drs. Romain Cartoni and Chantell Evans for critical feedback about the manuscript. We thank Sarah Johnson, Gracie Manigault, and Donna Porter for their excellent technical help. This work was supported by a Paul and Daisy Soros Fellowship (2020) and an HHMI Gilliam Fellowship (GT15076) to MPRS, a Chan Zuckerberg Initiative Neurodegeneration Challenge Network Collaborative grant (DAF2018-191999 and DAF2021-237435) to CE, an N.I.H. grant U19-NS123719 to CE and GY, and by the joint efforts of MJFF and the Aligning Science Across Parkinson's (ASAP) initiative. MJFF administers the grant ASAP-020607 to CE for ASAP and the Michael J Fox Foundation. Dr. Cagla Eroglu is an HHMI Investigator.

IP RIGHTS NOTICE

This article is subject to HHMI's Open Access to Publications policy. HHMI lab heads have previously granted a nonexclusive CC BY 4.0 license to the public and a sublicensable license to HHMI in their research articles. Pursuant to those licenses, the author-accepted manuscript of this article can be made freely available under a CC BY 4.0 license immediately upon publication.

AUTHOR CONTRIBUTIONS

Conceptualization, MPRS and CE; Methodology, MPRS, SK, VR, BL; Investigation, MPRS, SK, VR, GS; Formal analysis, MPR, SK, VR; Resources, MPRS, BL, GY, HS; Writing – original draft, MPRS, SK, CE; Writing – Review & Editing, MPRS, SK, VR, BL, GS, HS, GY, CE; Funding Acquisition, MPRS, GY, and CE.

bioRxiv preprint doi: https://doi.org/10.1101/2024.10.22.619706; this version posted October 23, 2024. The copyright holder for this preprint (which was not certified by peer review) is the author/funder, who has granted bioRxiv a license to display the preprint in perpetuity. It is made available under aCC-BY-NC-ND 4.0 International license.

REFERENCES

Abati, E., A. Manini, D. Velardo, R. Del Bo, L. Napoli, F. Rizzo, M. Moggio, N. Bresolin, E. Bellone, M.T. Bassi, M.G. D'Angelo, G.P. Comi, and S. Corti. 2022. Clinical and genetic features of a cohort of patients with MFN2-related neuropathy. *Scientific Reports*. 12:6181.

Agarwal, A., P.H. Wu, E.G. Hughes, M. Fukaya, M.A. Tischfield, A.J. Langseth, D. Wirtz, and D.E. Bergles. 2017. Transient Opening of the Mitochondrial Permeability Transition Pore Induces Microdomain Calcium Transients in Astrocyte Processes. *Neuron*. 93:587-605.e587.

Allen, N.J., and D.A. Lyons. 2018. Glia as architects of central nervous system formation and function. *Science*. 362:181-185.

Alvarez, J.I., T. Katayama, and A. Prat. 2013. Glial influence on the blood brain barrier. *Glia*. 61:1939-1958.

Baldwin, K.T., C.X. Tan, S.T. Strader, C. Jiang, J.T. Savage, X. Elorza-Vidal, X. Contreras, T. Rülicke, S. Hippenmeyer, R. Estévez, R.R. Ji, and C. Eroglu. 2021. HepaCAM controls astrocyte self-organization and coupling. *Neuron*. 109:2427-2442.e2410.

Billups, B., and I.D. Forsythe. 2002. Presynaptic Mitochondrial Calcium Sequestration Influences Transmission at Mammalian Central Synapses. *The Journal of Neuroscience*. 22:5840.

Bushong, E.A., M.E. Martone, and M.H. Ellisman. 2004. Maturation of astrocyte morphology and the establishment of astrocyte domains during postnatal hippocampal development. *International Journal of Developmental Neuroscience*. 22:73-86.

Bushong, E.A., M.E. Martone, Y.Z. Jones, and M.H. Ellisman. 2002. Protoplasmic astrocytes in CA1 stratum radiatum occupy separate anatomical domains. *J Neurosci*. 22:183-192.

Casillas-Espinosa, P.M., K.L. Powell, and T.J. O'Brien. 2012. Regulators of synaptic transmission: roles in the pathogenesis and treatment of epilepsy. *Epilepsia*. 53 Suppl 9:41-58.

Chang, C.-R., and C. Blackstone. 2010. Dynamic regulation of mitochondrial fission through modification of the dynamin-related protein Drp1. *Annals of the New York Academy of Sciences*. 1201:34.

Chen, F., and J. LoTurco. 2012. A method for stable transgenesis of radial glia lineage in rat neocortex by piggyBac mediated transposition. *J Neurosci Methods*. 207:172-180.

Chen, H., S.A. Detmer, A.J. Ewald, E.E. Griffin, S.E. Fraser, and D.C. Chan. 2003. Mitofusins Mfn1 and Mfn2 coordinately regulate mitochondrial fusion and are essential for embryonic development. *J Cell Biol*. 160:189-200.

Cheung, G., O. Chever, A. Rollenhagen, N. Quenech'du, P. Ezan, J.H.R. Lübke, and N. Rouach. 2023. Astroglial Connexin 43 Regulates Synaptic Vesicle Release at Hippocampal Synapses. *Cells*. 12.

Chih, B., L. Gollan, and P. Scheiffele. 2006. Alternative splicing controls selective trans-synaptic interactions of the neuroligin-neurexin complex. *Neuron*. 51:171-178.

Chung, W.S., N.J. Allen, and C. Eroglu. 2015. Astrocytes Control Synapse Formation, Function, and Elimination. *Cold Spring Harb Perspect Biol*. 7:a020370.

Clasadonte, J., E. Scemes, Z. Wang, D. Boison, and P.G. Haydon. 2017. Connexin 43-Mediated Astroglial Metabolic Networks Contribute to the Regulation of the Sleep-Wake Cycle. *Neuron*. 95:1365-1380.e1365.

Clavreul, S., L. Abdeladim, E. Hernández-Garzón, D. Niculescu, J. Durand, S.-H. Ieng, R. Barry, G. Bonvento, E. Beaurepaire, J. Livet, and K. Loulier. 2019. Cortical astrocytes develop in a plastic manner at both clonal and cellular levels. *Nature Communications*. 10:4884.

bioRxiv preprint doi: https://doi.org/10.1101/2024.10.22.619706; this version posted October 23, 2024. The copyright holder for this preprint (which was not certified by peer review) is the author/funder, who has granted bioRxiv a license to display the preprint in perpetuity. It is made available under aCC-BY-NC-ND 4.0 International license.

1046 Courchet, J., T.L. Lewis, Jr., S. Lee, V. Courchet, D.Y. Liou, S. Aizawa, and F. Polleux. 2013. Terminal
1047 axon branching is regulated by the LKB1-NUAK1 kinase pathway via presynaptic
1048 mitochondrial capture. *Cell*. 153:1510-1525.
1049 Cunniff, B., A.J. McKenzie, N.H. Heintz, and A.K. Howe. 2016. AMPK activity regulates trafficking of
1050 mitochondria to the leading edge during cell migration and matrix invasion. *Molecular biology*
1051 *of the cell*. 27:2662-2674.
1052 Dermietzel, R., E.L. Hertberg, J.A. Kessler, and D.C. Spray. 1991. Gap junctions between cultured
1053 astrocytes: immunocytochemical, molecular, and electrophysiological analysis. *J Neurosci*.
1054 11:1421-1432.
1055 Fahrner, J.A., R. Liu, M.S. Perry, J. Klein, and D.C. Chan. 2016. A novel de novo dominant negative
1056 mutation in DNM1L impairs mitochondrial fission and presents as childhood epileptic
1057 encephalopathy. *Am J Med Genet A*. 170:2002-2011.
1058 Fiebig, C., S. Keiner, B. Ebert, I. Schäffner, R. Jagasia, D.C. Lie, and R. Beckervordersandforth. 2019.
1059 Mitochondrial Dysfunction in Astrocytes Impairs the Generation of Reactive Astrocytes and
1060 Enhances Neuronal Cell Death in the Cortex Upon Photothrombotic Lesion. *Frontiers in*
1061 *molecular neuroscience*. 12:40-40.
1062 Fonseca, T.B., Á. Sánchez-Guerrero, I. Milosevic, and N. Raimundo. 2019. Mitochondrial fission
1063 requires DRP1 but not dynamins. *Nature*. 570:E34-E42.
1064 Fransson, Å., A. Ruusala, and P. Aspenström. 2006. The atypical Rho GTPases Miro-1 and Miro-2 have
1065 essential roles in mitochondrial trafficking. *Biochemical and biophysical research*
1066 *communications*. 344:500-510.
1067 Friedman, J.R., and J. Nunnari. 2014. Mitochondrial form and function. *Nature*. 505:335-343.
1068 Giaume, C., A. Koulakoff, L. Roux, D. Holcman, and N. Rouach. 2010. Astroglial networks: a step
1069 further in neuroglial and gliovascular interactions. *Nat Rev Neurosci*. 11:87-99.
1070 Gollihue, J.L., and C.M. Norris. 2020. Astrocyte mitochondria: Central players and potential
1071 therapeutic targets for neurodegenerative diseases and injury. *Ageing Res Rev*. 59:101039.
1072 Göbel, J., P. Pelzer, E. Engelhardt, V. Sakthivelu, H.M. Jahn, M. Jevtic, K. Folz-Donahue, C. Kukat, A.
1073 Schauss, C.K. Frese, A. Ghanem, K.-K. Conzelmann, E. Motori, and M. Bergami. 2019.
1074 Mitochondrial fusion in reactive astrocytes coordinates local metabolic domains to promote
1075 vascular repair. *bioRxiv*:657999.
1076 Haseleu, J., E. Anlauf, S. Blaess, E. Endl, and A. Derouiche. 2013. Studying subcellular detail in fixed
1077 astrocytes: dissociation of morphologically intact glial cells (DIMIGs). *Frontiers in Cellular*
1078 *Neuroscience*. 7.
1079 Holt, L.M., R.D. Hernandez, N.L. Pacheco, B. Torres Ceja, M. Hossain, and M.L. Olsen. 2019.
1080 Astrocyte morphogenesis is dependent on BDNF signaling via astrocytic TrkB.T1. *Elife*. 8.
1081 Hösli, L., N. Binini, K.D. Ferrari, L. Thieren, Z.J. Looser, M. Zuend, H.S. Zanker, S. Berry, M. Holub, W.
1082 Möbius, T. Ruhwedel, K.A. Nave, C. Giaume, B. Weber, and A.S. Saab. 2022. Decoupling
1083 astrocytes in adult mice impairs synaptic plasticity and spatial learning. *Cell Rep*. 38:110484.
1084 Ignatenko, O., D. Chilov, I. Paetau, E. de Miguel, C.B. Jackson, G. Capin, A. Paetau, M. Terzioglu, L.
1085 Euro, and A. Suomalainen. 2018. Loss of mtDNA activates astrocytes and leads to spongiotic
1086 encephalopathy. *Nature Communications*. 9:70.
1087 Kameritsch, P., K. Pogoda, and U. Pohl. 2012. Channel-independent influence of connexin 43 on cell
1088 migration. *Biochim Biophys Acta*. 1818:1993-2001.
1089 Ke, P., J. Gu, J. Liu, Y. Liu, X. Tian, Y. Ma, Y. Meng, and F. Xiao. 2023. Syntabulin regulates neuronal
1090 excitation/inhibition balance and epileptic seizures by transporting syntaxin 1B. *Cell Death*
1091 *Discov*. 9:187.

bioRxiv preprint doi: https://doi.org/10.1101/2024.10.22.619706; this version posted October 23, 2024. The copyright holder for this preprint (which was not certified by peer review) is the author/funder, who has granted bioRxiv a license to display the preprint in perpetuity. It is made available under aCC-BY-NC-ND 4.0 International license.

König, T., H. Nolte, M.J. Aaltonen, T. Tatsuta, M. Krols, T. Stroh, T. Langer, and H.M. McBride. 2021. MIROs and DRP1 drive mitochondrial-derived vesicle biogenesis and promote quality control. *Nat Cell Biol*. 23:1271-1286.

Lagos-Cabré, R., F. Burgos-Bravo, A.M. Avalos, and L. Leyton. 2019. Connexins in Astrocyte Migration. *Front Pharmacol*. 10:1546.

Lhuissier, C., B.E. Wagner, A. Vincent, G. Garraux, O. Hougrand, R. Van Coster, V. Benoit, D. Karadurmus, G. Lenaers, N. Gueguen, A. Chevrollier, and I. Maystadt. 2022. Case report: Thirty-year progression of an EMPF1 encephalopathy due to defective mitochondrial and peroxisomal fission caused by a novel de novo heterozygous DNM1L variant. *Front Neurol*. 13:937885.

Li, Z., K. Okamoto, Y. Hayashi, and M. Sheng. 2004. The importance of dendritic mitochondria in the morphogenesis and plasticity of spines and synapses. *Cell*. 119:873-887.

Liu, X., Z. Zhang, D. Li, M. Lei, Q. Li, and P. Zhang. 2021. DNM1L-Related Mitochondrial Fission Defects Presenting as Encephalopathy: A Case Report and Literature Review. *Front Pediatr*. 9:626657.

Losón, O.C., Z. Song, H. Chen, and D.C. Chan. 2013. Fis1, Mff, MiD49, and MiD51 mediate Drp1 recruitment in mitochondrial fission. *Molecular biology of the cell*. 24:659-667.

Lovatt, D., U. Sonnewald, H.S. Waagepetersen, A. Schousboe, W. He, J.H.C. Lin, X. Han, T. Takano, S. Wang, F.J. Sim, S.A. Goldman, and M. Nedergaard. 2007. The Transcriptome and Metabolic Gene Signature of Protoplasmic Astrocytes in the Adult Murine Cortex. *The Journal of Neuroscience*. 27:12255.

López-Doménech, G., Nathalie F. Higgs, V. Vaccaro, H. Roš, I.L. Arancibia-Cárcamo, Andrew F. MacAskill, and Josef T. Kittler. 2016. Loss of Dendritic Complexity Precedes Neurodegeneration in a Mouse Model with Disrupted Mitochondrial Distribution in Mature Dendrites. *Cell Reports*. 17:317-327.

López-Doménech, G., and J.T. Kittler. 2023. Mitochondrial regulation of local supply of energy in neurons. *Curr Opin Neurobiol*. 81:102747.

Middeldorp, J., and E.M. Hol. 2011. GFAP in health and disease. *Progress in Neurobiology*. 93:421-443.

Moffat, J., D.A. Grueneberg, X. Yang, S.Y. Kim, A.M. Kloepfer, G. Hinkle, B. Piqani, T.M. Eisenhaure, B. Luo, J.K. Grenier, A.E. Carpenter, S.Y. Foo, S.A. Stewart, B.R. Stockwell, N. Hacohen, W.C. Hahn, E.S. Lander, D.M. Sabatini, and D.E. Root. 2006. A lentiviral RNAi library for human and mouse genes applied to an arrayed viral high-content screen. *Cell*. 124:1283-1298.

Motori, E., J. Puyal, N. Toni, A. Ghanem, C. Angeloni, M. Malaguti, G. Cantelli-Forti, B. Berninger, K.-K. Conzelmann, M. Götz, Konstanze F. Winklhofer, S. Hrelia, and M. Bergami. 2013. Inflammation-Induced Alteration of Astrocyte Mitochondrial Dynamics Requires Autophagy for Mitochondrial Network Maintenance. *Cell Metabolism*. 18:844-859.

Ni, H.M., J.A. Williams, and W.X. Ding. 2015. Mitochondrial dynamics and mitochondrial quality control. *Redox Biol*. 4:6-13.

Oberheim, N.A., G.F. Tian, X. Han, W. Peng, T. Takano, B. Ransom, and M. Nedergaard. 2008. Loss of astrocytic domain organization in the epileptic brain. *J Neurosci*. 28:3264-3276.

Pellerin, L., and P.J. Magistretti. 1994. Glutamate uptake into astrocytes stimulates aerobic glycolysis: a mechanism coupling neuronal activity to glucose utilization. *Proc Natl Acad Sci U S A*. 91:10625-10629.

Pellerin, L., G. Pellegri, P.G. Bittar, Y. Charnay, C. Bouras, J.L. Martin, N. Stella, and P.J. Magistretti. 1998. Evidence supporting the existence of an activity-dependent astrocyte-neuron lactate shuttle. *Dev Neurosci*. 20:291-299.

bioRxiv preprint doi: https://doi.org/10.1101/2024.10.22.619706; this version posted October 23, 2024. The copyright holder for this preprint (which was not certified by peer review) is the author/funder, who has granted bioRxiv a license to display the preprint in perpetuity. It is made available under aCC-BY-NC-ND 4.0 International license.

1139 Popov, A., N. Brazhe, K. Morozova, K. Yashin, M. Bychkov, O. Nosova, O. Sutyagina, A. Brazhe, E.
1140 Parshina, L. Li, I. Medyanik, D.E. Korzhevskii, Z. Shenkarev, E. Lyukmanova, A. Verkhratsky,
1141 and A. Semyanov. 2023. Mitochondrial malfunction and atrophy of astrocytes in the aged
1142 human cerebral cortex. *Nature Communications*. 14:8380.
1143 Rangaraju, V., M. Lauterbach, and E.M. Schuman. 2019. Spatially Stable Mitochondrial
1144 Compartments Fuel Local Translation during Plasticity. *Cell*. 176:73-84.e15.
1145 Rash, J.E., T. Yasumura, F.E. Dudek, and J.I. Nagy. 2001. Cell-specific expression of connexins and
1146 evidence of restricted gap junctional coupling between glial cells and between neurons. *J*
1147 *Neurosci*. 21:1983-2000.
1148 Ren, D., P. Zheng, J. Feng, Y. Gong, Y. Wang, J. Duan, L. Zhao, J. Deng, H. Chen, S. Zou, T. Hong, and
1149 W. Chen. 2020. Overexpression of Astrocytes-Specific GJA1-20k Enhances the Viability and
1150 Recovery of the Neurons in a Rat Model of Traumatic Brain Injury. *ACS Chemical*
1151 *Neuroscience*. 11:1643-1650.
1152 Shimura, D., E. Nuebel, R. Baum, S.E. Valdez, S. Xiao, J.S. Warren, J.A. Palatinus, T. Hong, J. Rutter,
1153 and R.M. Shaw. 2021. Protective mitochondrial fission induced by stress-responsive protein
1154 GJA1-20k. *Elife*. 10.
1155 Smirnova, E., L. Griparic, D.L. Shurland, and A.M. van der Bliek. 2001. Dynamin-related protein Drp1
1156 is required for mitochondrial division in mammalian cells. *Mol Biol Cell*. 12:2245-2256.
1157 Smith, G.M., and G. Gallo. 2018. The role of mitochondria in axon development and regeneration.
1158 *Developmental neurobiology*. 78:221-237.
1159 Smyth, J.W., and R.M. Shaw. 2013. Autoregulation of connexin43 gap junction formation by internally
1160 translated isoforms. *Cell Rep*. 5:611-618.
1161 Srinivasan, R., T.Y. Lu, H. Chai, J. Xu, B.S. Huang, P. Golshani, G. Coppola, and B.S. Khakh. 2016. New
1162 Transgenic Mouse Lines for Selectively Targeting Astrocytes and Studying Calcium Signals in
1163 Astrocyte Processes In Situ and In Vivo. *Neuron*. 92:1181-1195.
1164 Steketee, M.B., S.N. Moysidis, J.E. Weinstein, A. Kreymerman, J.P. Silva, S. Iqbal, and J.L. Goldberg.
1165 2012. Mitochondrial dynamics regulate growth cone motility, guidance, and neurite growth
1166 rate in perinatal retinal ganglion cells in vitro. *Invest Ophthalmol Vis Sci*. 53:7402-7411.
1167 Stephen, T.L., N.F. Higgs, D.F. Sheehan, S. Al Awabdh, G. Lopez-Domenech, I.L. Arancibia-Carcamo,
1168 and J.T. Kittler. 2015. Miro1 Regulates Activity-Driven Positioning of Mitochondria within
1169 Astrocytic Processes Apposed to Synapses to Regulate Intracellular Calcium Signaling. *J*
1170 *Neurosci*. 35:15996-16011.
1171 Stogsdill, J.A., J. Ramirez, D. Liu, Y.-H. Kim, K.T. Baldwin, E. Enustun, T. Ejikeme, R.-R. Ji, and C. Eroglu.
1172 2017. Astrocytic Neuroligins Control Astrocyte Morphogenesis and Synaptogenesis. *Nature*.
1173 551:192-197.
1174 Supplie, L.M., T. Düking, G. Campbell, F. Diaz, C.T. Moraes, M. Götz, B. Hamprecht, S. Boretius, D.
1175 Mahad, and K.-A. Nave. 2017. Respiration-Deficient Astrocytes Survive As Glycolytic Cells
1176 In Vivo. *The Journal of Neuroscience*. 37:4231.
1177 Takano, T., J.T. Wallace, K.T. Baldwin, A.M. Purkey, A. Uezu, J.L. Courtland, E.J. Soderblom, T.
1178 Shimogori, P.F. Maness, C. Eroglu, and S.H. Soderling. 2020. Chemico-genetic discovery of
1179 astrocytic control of inhibition in vivo. *Nature*. 588:296-302.
1180 Tan, C.X., D.S. Bindu, E.J. Hardin, K. Sakers, R. Baumert, J.J. Ramirez, J.T. Savage, and C. Eroglu. 2023.
1181 δ-Catenin controls astrocyte morphogenesis via layer-specific astrocyte-neuron cadherin
1182 interactions. *J Cell Biol*. 222.
1183 Uo, T., J. Dworzak, C. Kinoshita, D.M. Inman, Y. Kinoshita, P.J. Horner, and R.S. Morrison. 2009. Drp1
1184 levels constitutively regulate mitochondrial dynamics and cell survival in cortical neurons.
1185 *Exp Neurol*. 218:274-285.

bioRxiv preprint doi: https://doi.org/10.1101/2024.10.22.619706; this version posted October 23, 2024. The copyright holder for this preprint (which was not certified by peer review) is the author/funder, who has granted bioRxiv a license to display the preprint in perpetuity. It is made available under aCC-BY-NC-ND 4.0 International license.

1186 Vanstone, J.R., A.M. Smith, S. McBride, T. Naas, M. Holcik, G. Antoun, M.-E. Harper, J. Michaud, E.
1187 Sell, P. Chakraborty, M. Tetreault, J. Majewski, S. Baird, K.M. Boycott, D.A. Dyment, A.
1188 MacKenzie, M.A. Lines, and C. Care4Rare. 2016. DNM1L-related mitochondrial fission defect
1189 presenting as refractory epilepsy. *European Journal of Human Genetics*. 24:1084-1088.
1190 Wakabayashi, J., Z. Zhang, N. Wakabayashi, Y. Tamura, M. Fukaya, T.W. Kensler, M. Iijima, and H.
1191 Sesaki. 2009a. The dynamin-related GTPase Drp1 is required for embryonic and brain
1192 development in mice. *J Cell Biol*. 186:805-816.
1193 Wakabayashi, J., Z. Zhang, N. Wakabayashi, Y. Tamura, M. Fukaya, T.W. Kensler, M. Iijima, and H.
1194 Sesaki. 2009b. The dynamin-related GTPase Drp1 is required for embryonic and brain
1195 development in mice. *The Journal of cell biology*. 186:805-816.
1196 Wang, Y., C. Wang, P. Ranefall, G.J. Broussard, G. Shi, B. Lyu, C.T. Wu, L. Tian, and G. Yu. 2020.
1197 SynQuant: an automatic tool to quantify synapses from microscopy images. *Bioinformatics*.
1198 36:1599-1606.
1199 Wiencken-Barger, A.E., B. Djukic, K.B. Casper, and K.D. McCarthy. 2007. A role for Connexin43 during
1200 neurodevelopment. *Glia*. 55:675-686.
1201 Xiao, S., D. Shimura, R. Baum, D.M. Hernandez, S. Agvanian, Y. Nagaoka, M. Katsumata, P.D. Lampe,
1202 A.G. Kleber, T. Hong, and R.M. Shaw. 2020. Auxiliary trafficking subunit GJA1-20k protects
1203 connexin-43 from degradation and limits ventricular arrhythmias. *The Journal of Clinical*
1204 *Investigation*. 130:4858-4870.
1205 Youle, R.J., and A.M. van der Bliek. 2012. Mitochondrial fission, fusion, and stress. *Science*.
1206 337:1062-1065.
1207 Zehnder, T., F. Petrelli, J. Romanos, E.C. De Oliveira Figueiredo, T.L. Lewis, Jr., N. Déglon, F. Polleux,
1208 M. Santello, and P. Bezzi. 2021. Mitochondrial biogenesis in developing astrocytes regulates
1209 astrocyte maturation and synapse formation. *Cell Rep*. 35:108952.
1210 Zipursky, S., J. Lee, A. Sergeeva, G. Ahlsen, S. Mannepalli, F. Bahna, K. Goodman, B. Khakh, J. Weiner,
1211 L. Shapiro, and B. Honig. 2024. Astrocyte morphogenesis requires self-recognition. *Res Sq*.

1212

Fig 1: Mitochondria increase in number and decrease in size during cortical astrocyte morphogenesis *in vivo.*

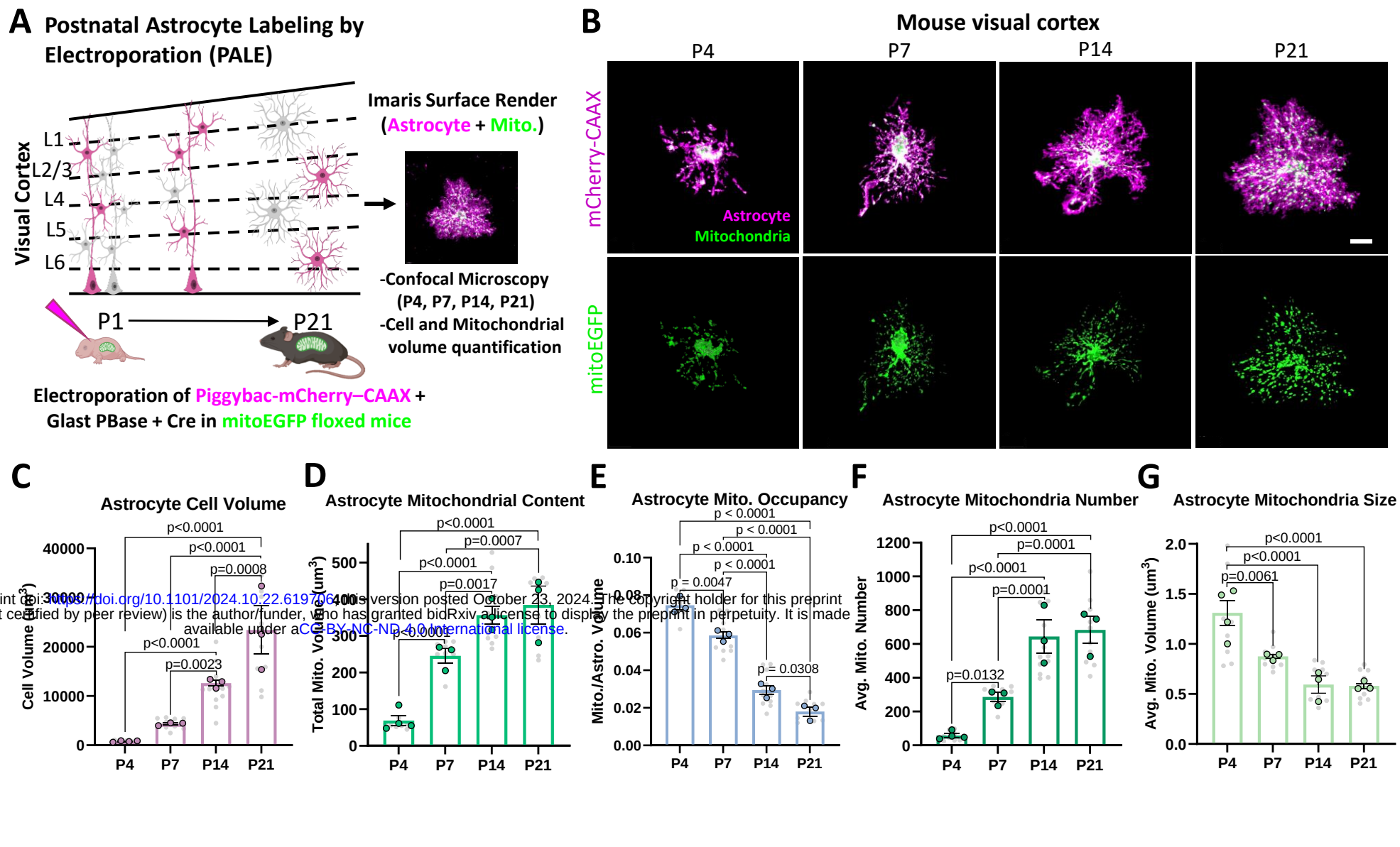

bioRxiv preprint doi: https://doi.org/10.1101/2024.10.22.619776; this version posted October 23, 2024. The copyright holder for this preprint (which was not certified by peer review) is the author/funder, who has granted bioRxiv a license to display the preprint in perpetuity. It is made available under aCC BY-NC-ND 4.0 International license.

Fig 2: Mitochondrial occupy fine astrocyte processes concurrently with astrocyte morphological arborization *in vitro.*

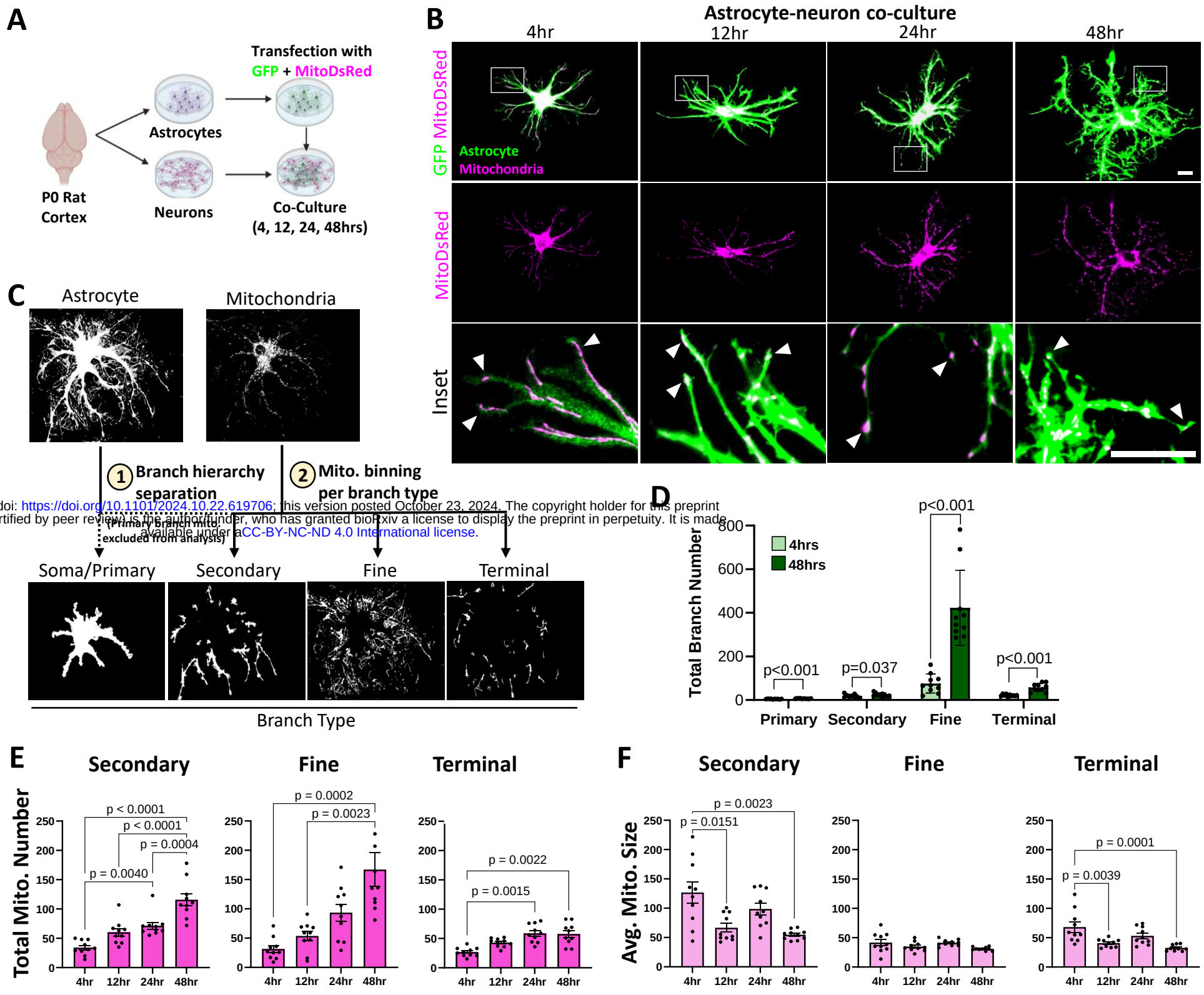

bioRxiv preprint doi: https://doi.org/10.1101/2024.10.22.619706; this version posted October 23, 2024. The copyright holder for this preprint (which was not certified by peer review) is the author/funder, who has granted bioRxiv a license to display the preprint in perpetuity. It is made available under aCC-BY-NC-ND 4.0 International license.

Fig 3: Drp1-induced mitochondrial fission is required for fine astrocyte process formation and mitochondrial localization *in vitro.*

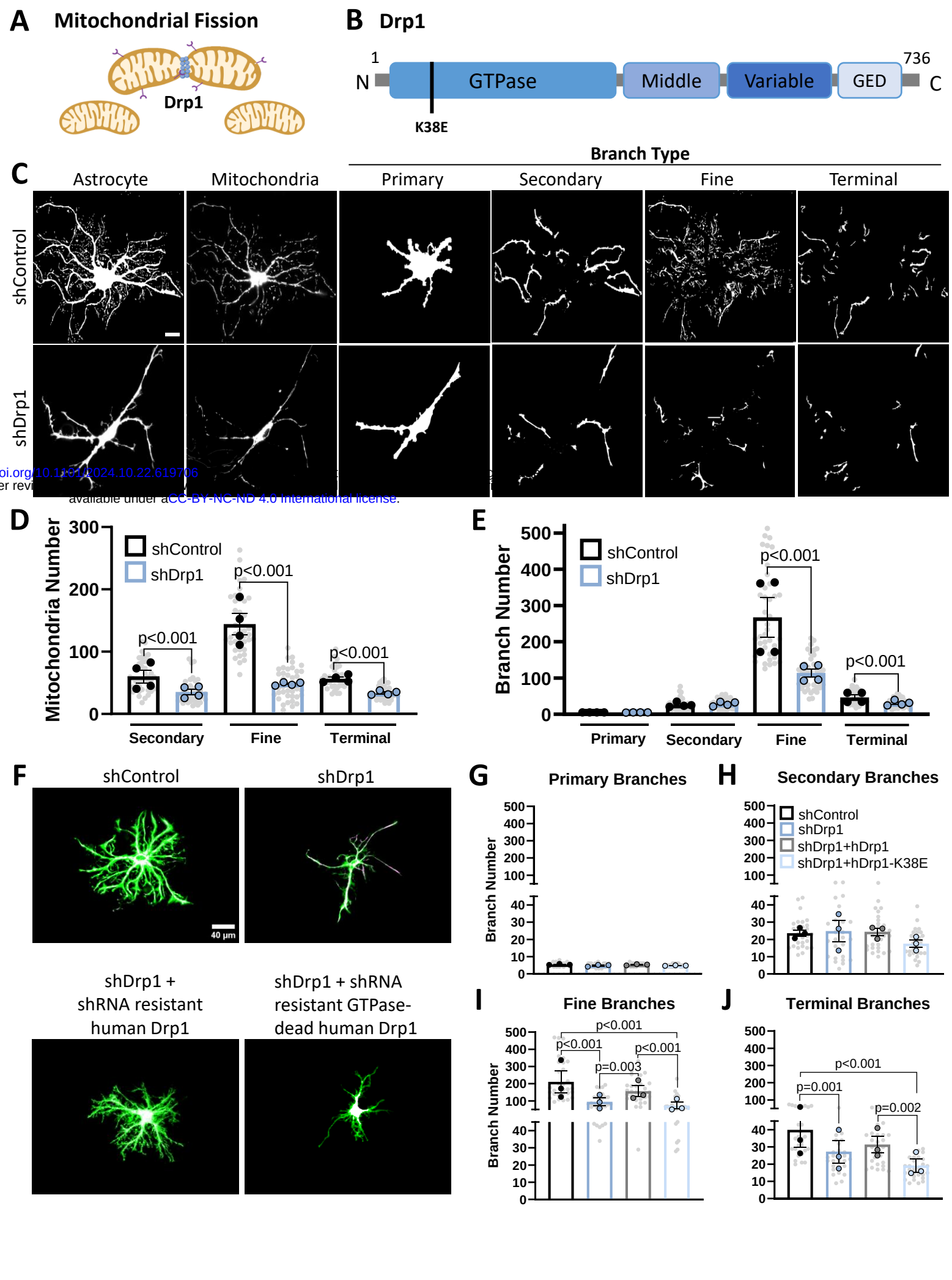

bioRxiv preprint doi: https://doi.org/10.1101/2024.10.22.619706
(which was not certified by peer revi
available under aCC-BY-NC-ND 4.0 International license.

Supplemental 1: Validation of shRNA tools

A

shDrp1	ms	CTATAATGCATGCACTATTTA
	rat	CTATAATGCATGCACTATTTA
	Hm	XXXXAATGCATGCACTATXXX

C

shMiro1	ms	TGGACTGTGCTTCGACGATTT
shMfn1	ms	GCAAGATTACAGGAGTTTCAA

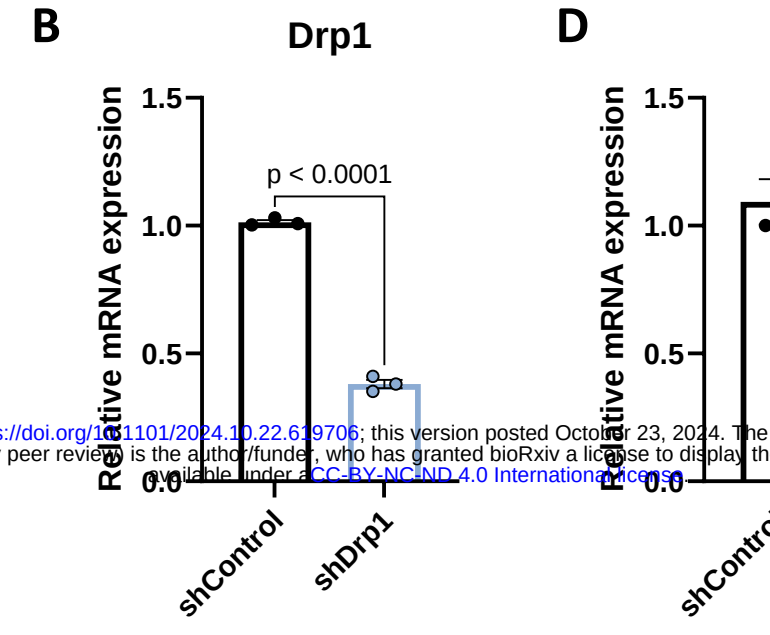

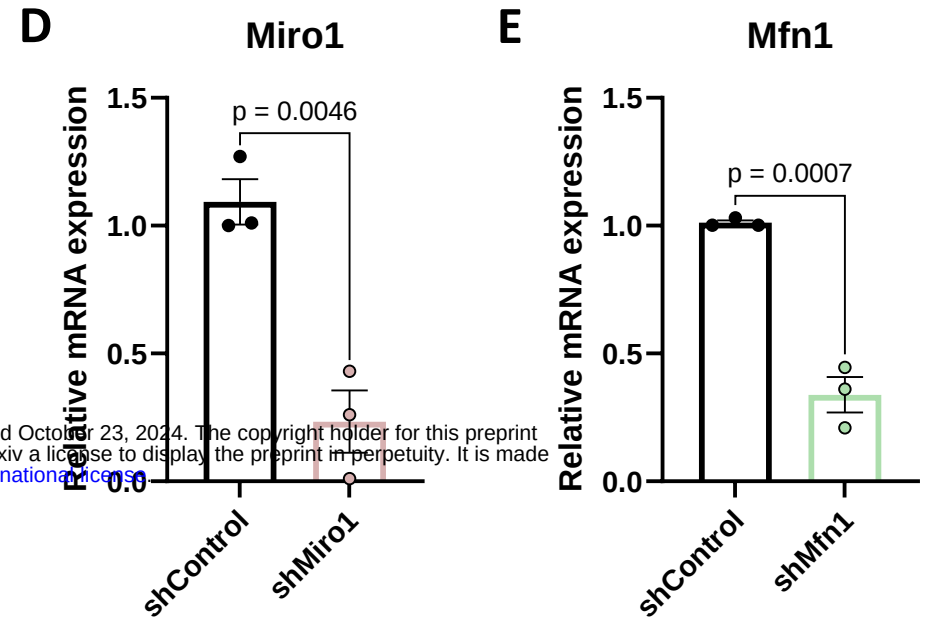

bioRxiv preprint doi: https://doi.org/10.1101/2024.10.22.619706; this version posted October 23, 2024. The copyright holder for this preprint (which was not certified by peer review) is the author/funder, who has granted bioRxiv a license to display the preprint in perpetuity. It is made available under aCC-BY-NC-ND 4.0 International license.

Fig 4: Mitochondrial fission, not fusion nor transport, is required for distal astrocyte process morphogenesis *in vivo*

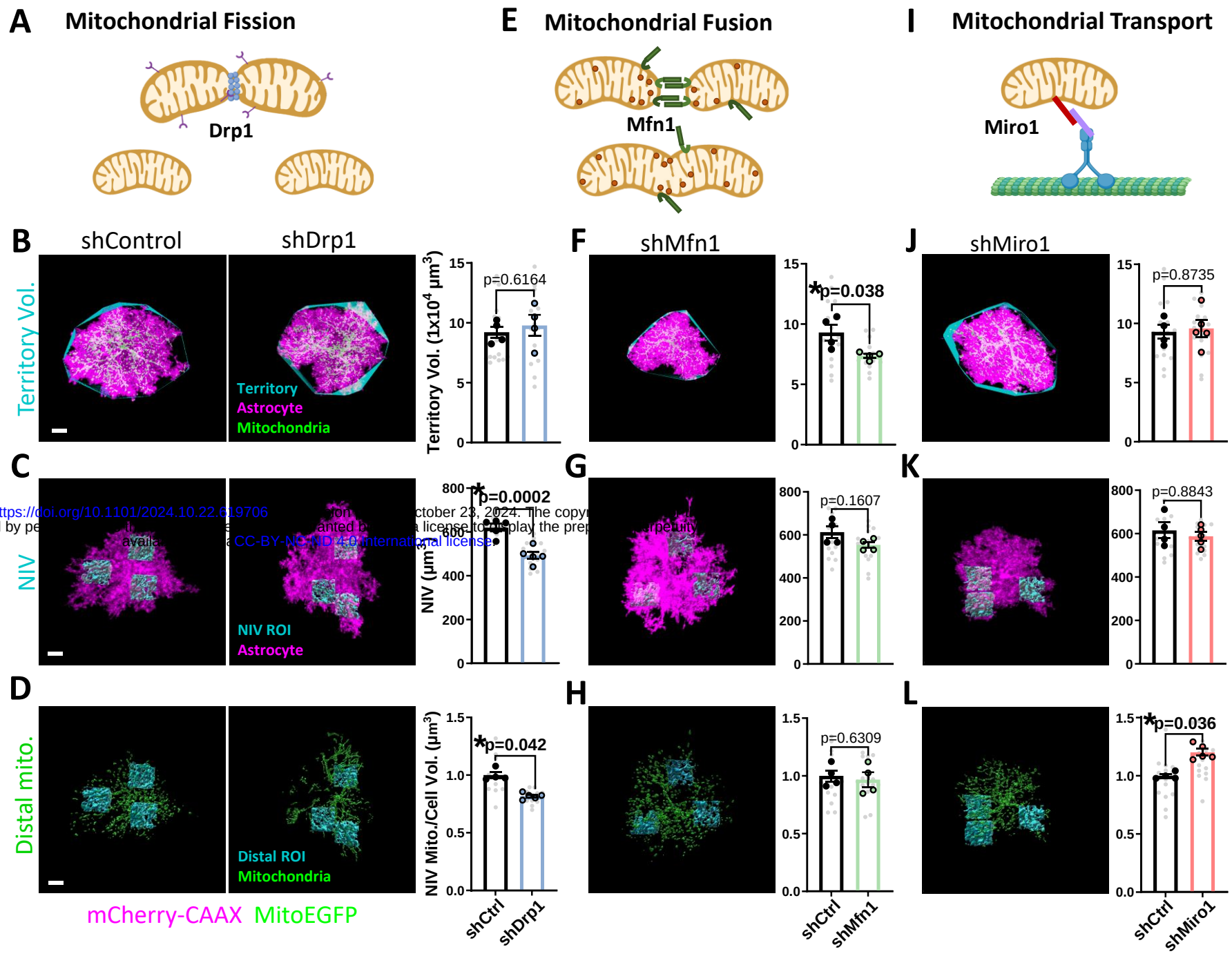

bioRxiv preprint doi: https://doi.org/10.1101/2024.10.22.619706
(which was not certified by pe
ctober 23, 2024. The copyr
a license to display the prep
CC-BY-NC-ND 4.0 International license

Supplemental 2: Mitochondrial dynamics do not affect astrocyte total mitochondrial content.

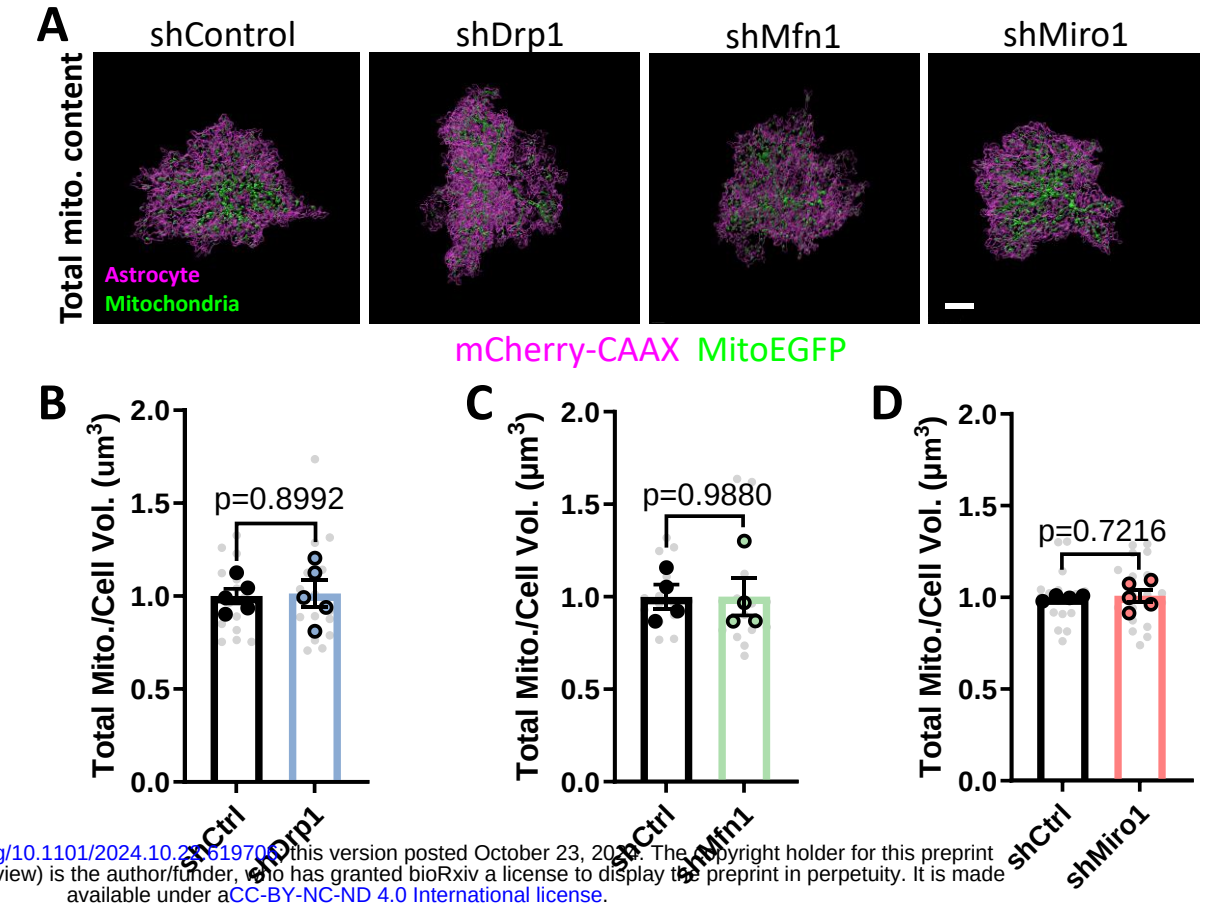

bioRxiv preprint doi: https://doi.org/10.1101/2024.10.23.619700 this version posted October 23, 2024. The copyright holder for this preprint (which was not certified by peer review) is the author/funder, who has granted bioRxiv a license to display the preprint in perpetuity. It is made available under aCC-BY-NC-ND 4.0 International license.

Fig 5: Drp1 controls cortical astrocyte organization during postnatal development

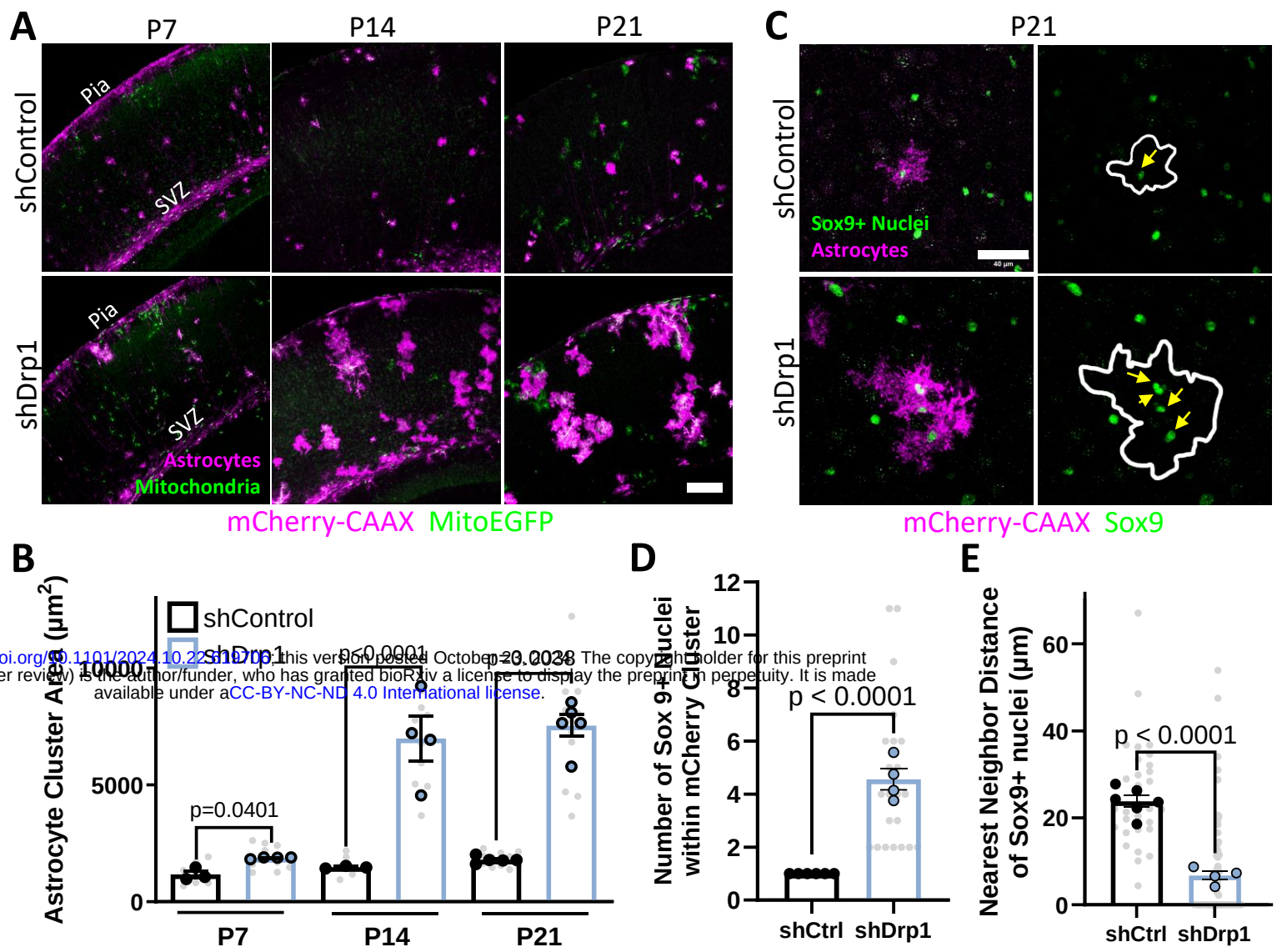

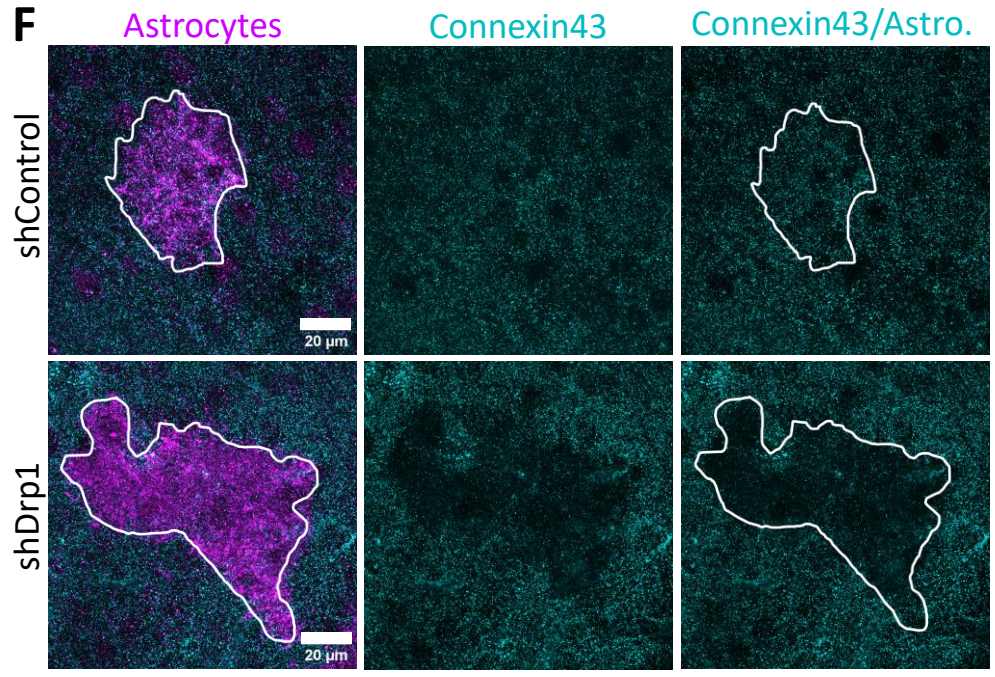

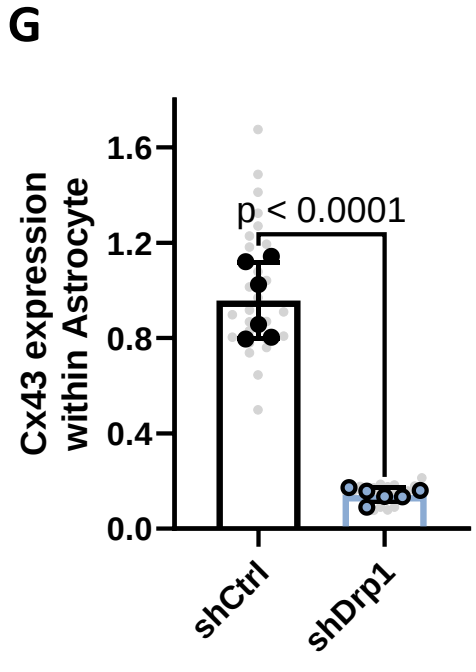

bioRxiv preprint doi: https://doi.org/10.1101/2024.10.22.619709; this version posted October 23, 2024. The copyright holder for this preprint (which was not certified by peer review) is the author/funder, who has granted bioRxiv a license to display the preprint in perpetuity. It is made available under aCC-BY-NC-ND 4.0 International license.

Supplemental 3: shDrp1-induced astrocyte clustering is not a result of increased astrocyte proliferation and is maintained through adulthood

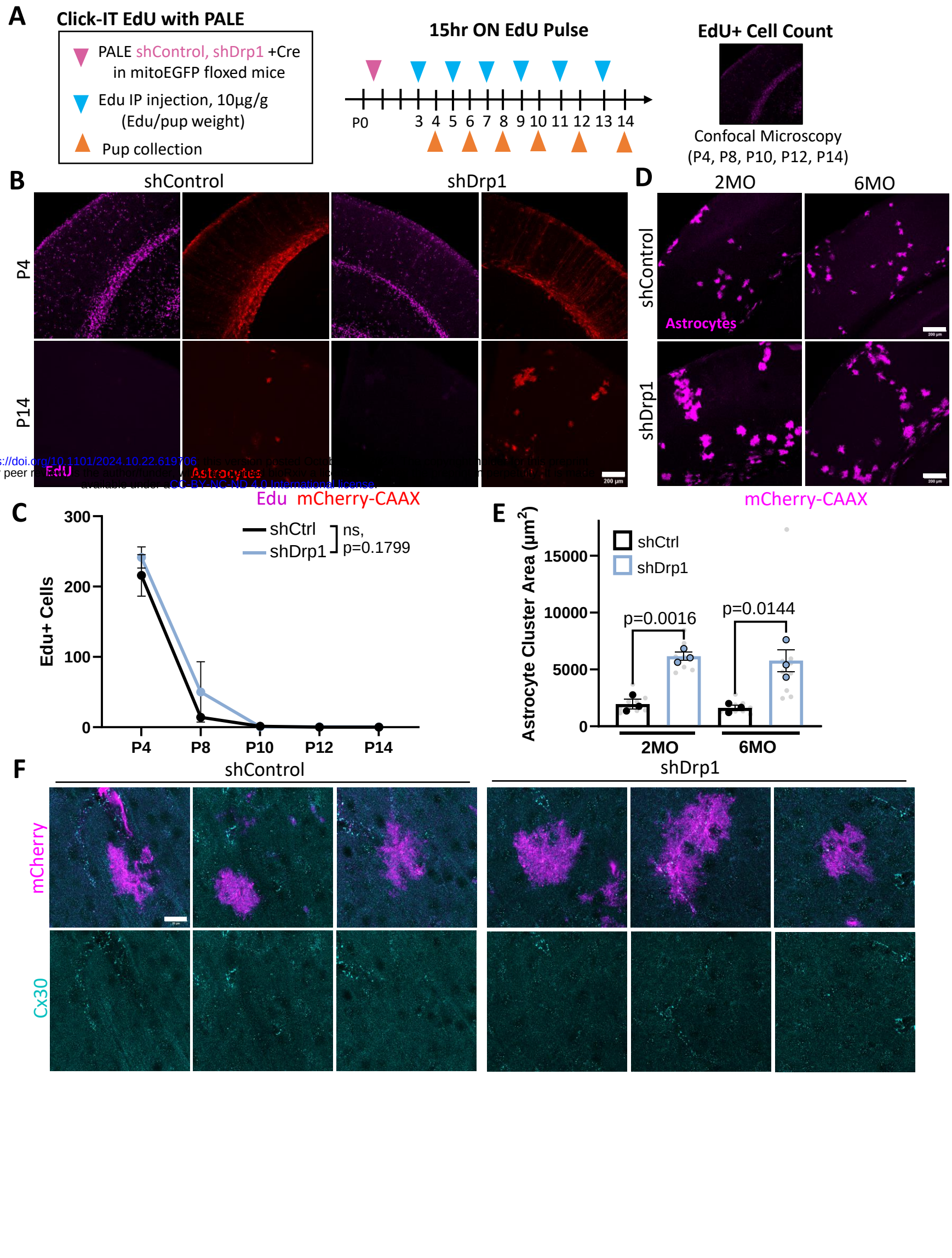

bioRxiv preprint doi: https://doi.org/10.1101/2024.10.22.619706 this version posted Oct
(which was not certified by peer r
the author/funder, w
bioRxiv a
CC-BY-NC-ND 4.0 International license.

Fig 6: Astrocyte-specific Drp1 cKO induces cortical astrocyte reactivity

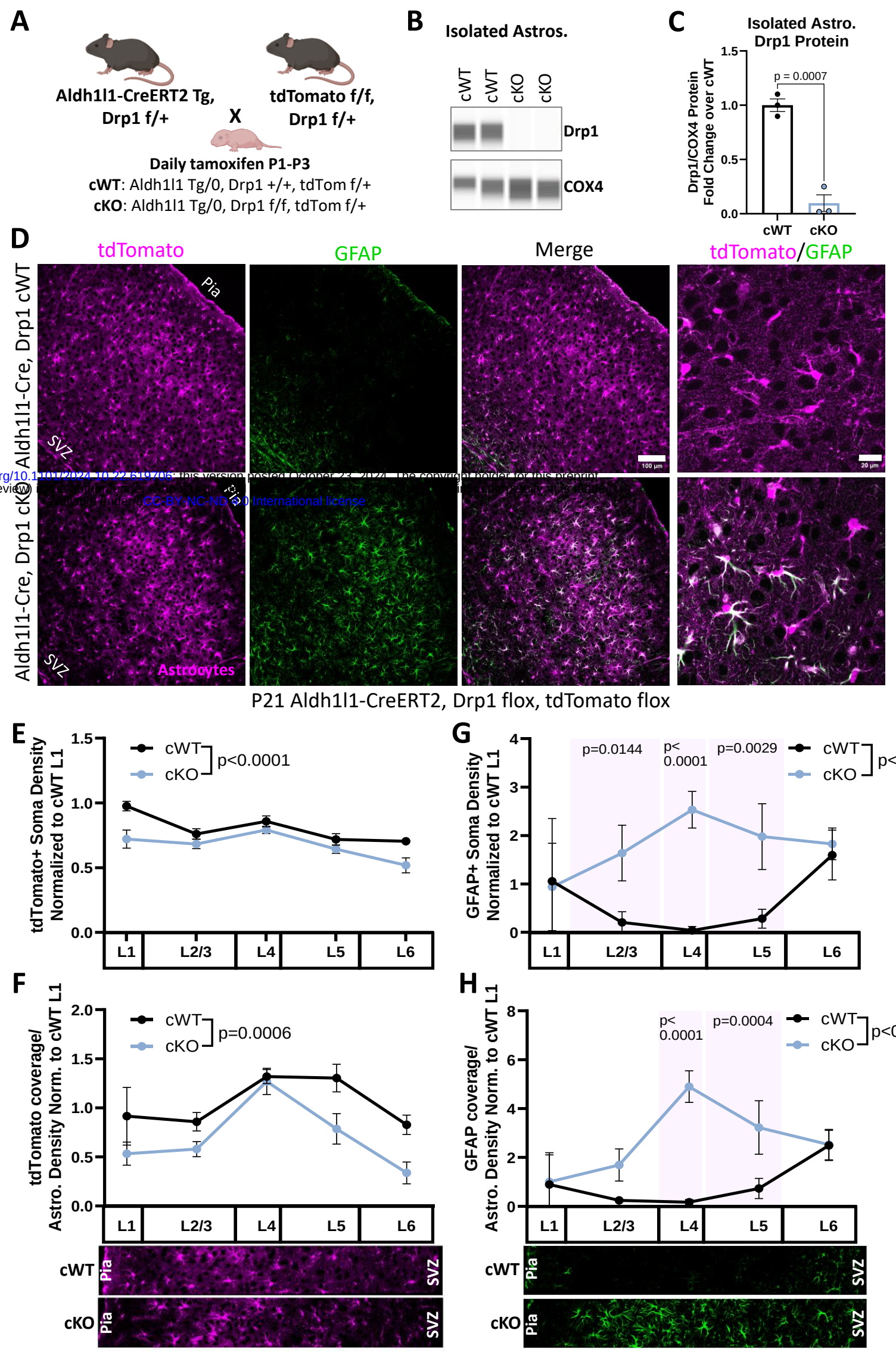

bioRxiv preprint doi: https://doi.org/10.1101/2024.10.22.619706; this version posted October 23, 2024. The copyright holder for this preprint (which was not certified by peer review) is the author/funder, who has granted bioRxiv a license to display the preprint in perpetuity. It is made available under aCC-BY-NC-ND 4.0 International license.

Supplemental 4: Astrocyte-Specific Drp1 cKO mouse characterization

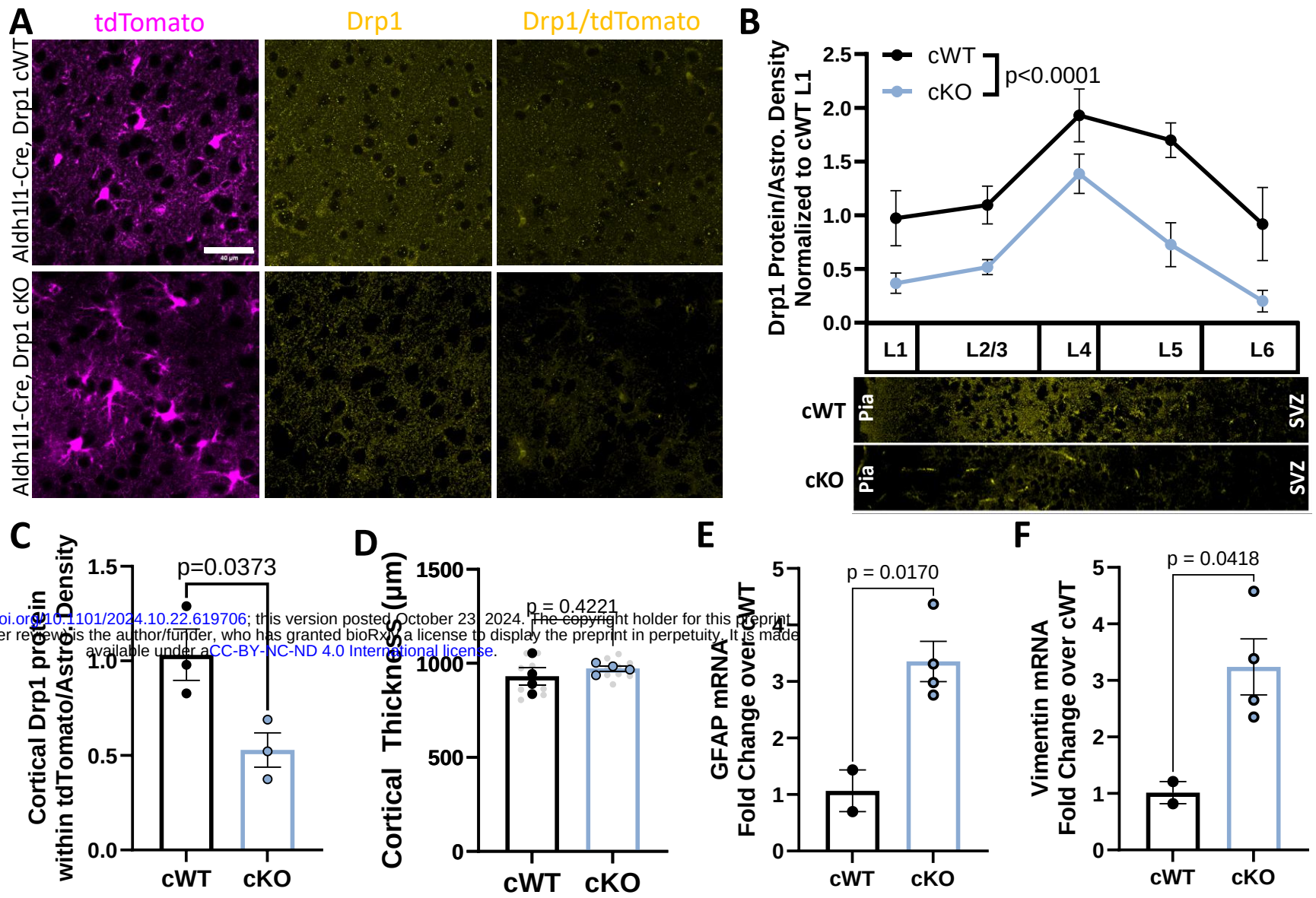

bioRxiv preprint doi: https://doi.org/10.1101/2024.10.22.619706; this version posted October 23, 2024. The copyright holder for this preprint (which was not certified by peer review) is the author/funder, who has granted bioRxiv a license to display the preprint in perpetuity. It is made available under aCC-BY-NC-ND 4.0 International license.

Fig 7: Astrocytic Drp1 loss dysregulates astrocyte organization and Connexin 43 expression in the mouse cortex

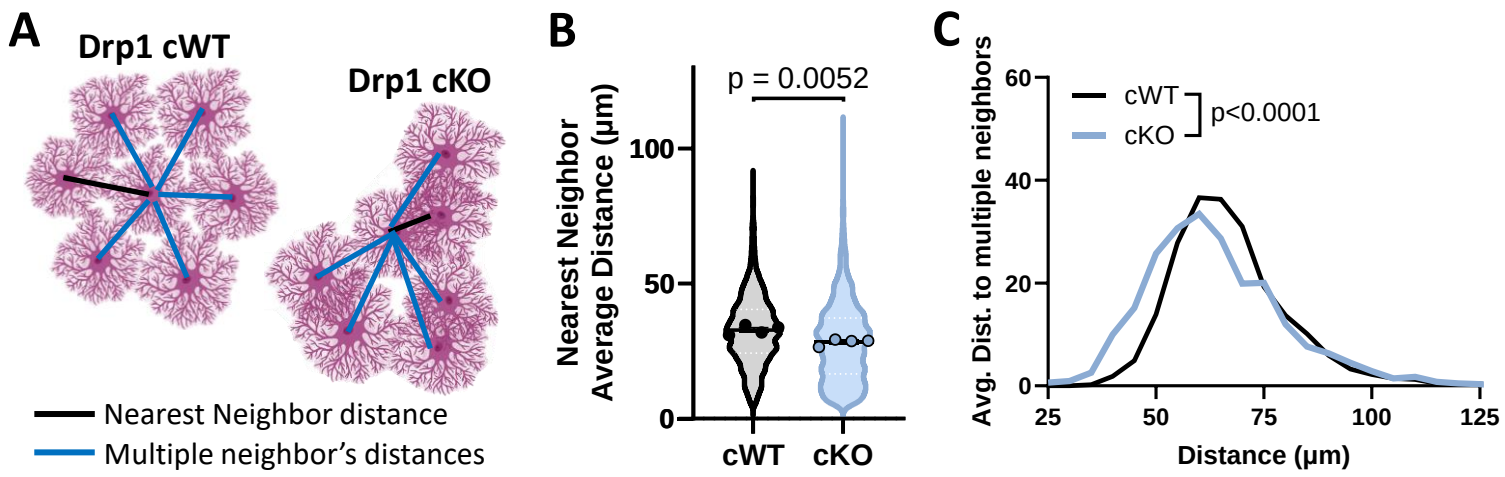

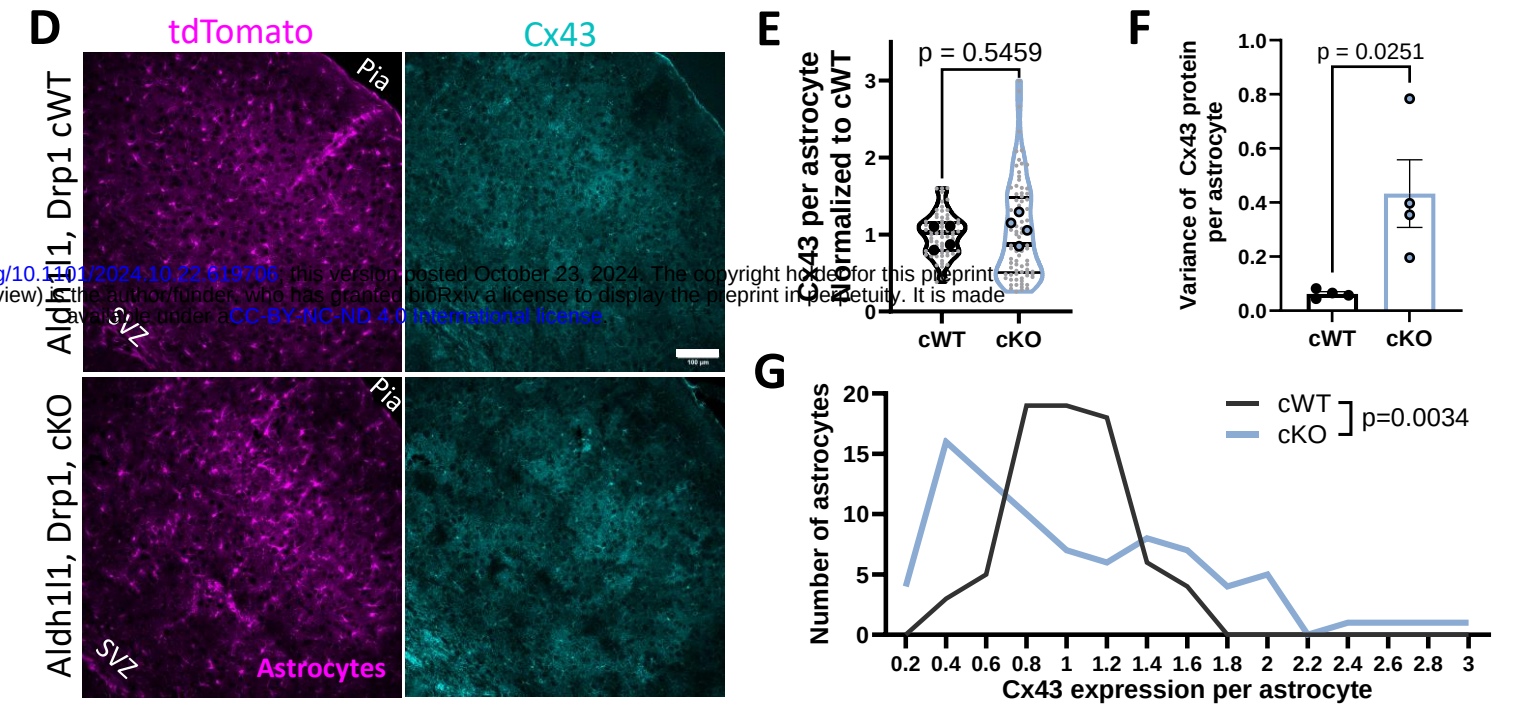

bioRxiv preprint doi: https://doi.org/10.1101/2024.10.22.619706 this version posted October 23, 2024. The copyright holder for this preprint (which was not certified by peer review) is the author/funder, who has granted bioRxiv a license to display the preprint in perpetuity. It is made available under a CC-BY-NC-ND 4.0 International license.